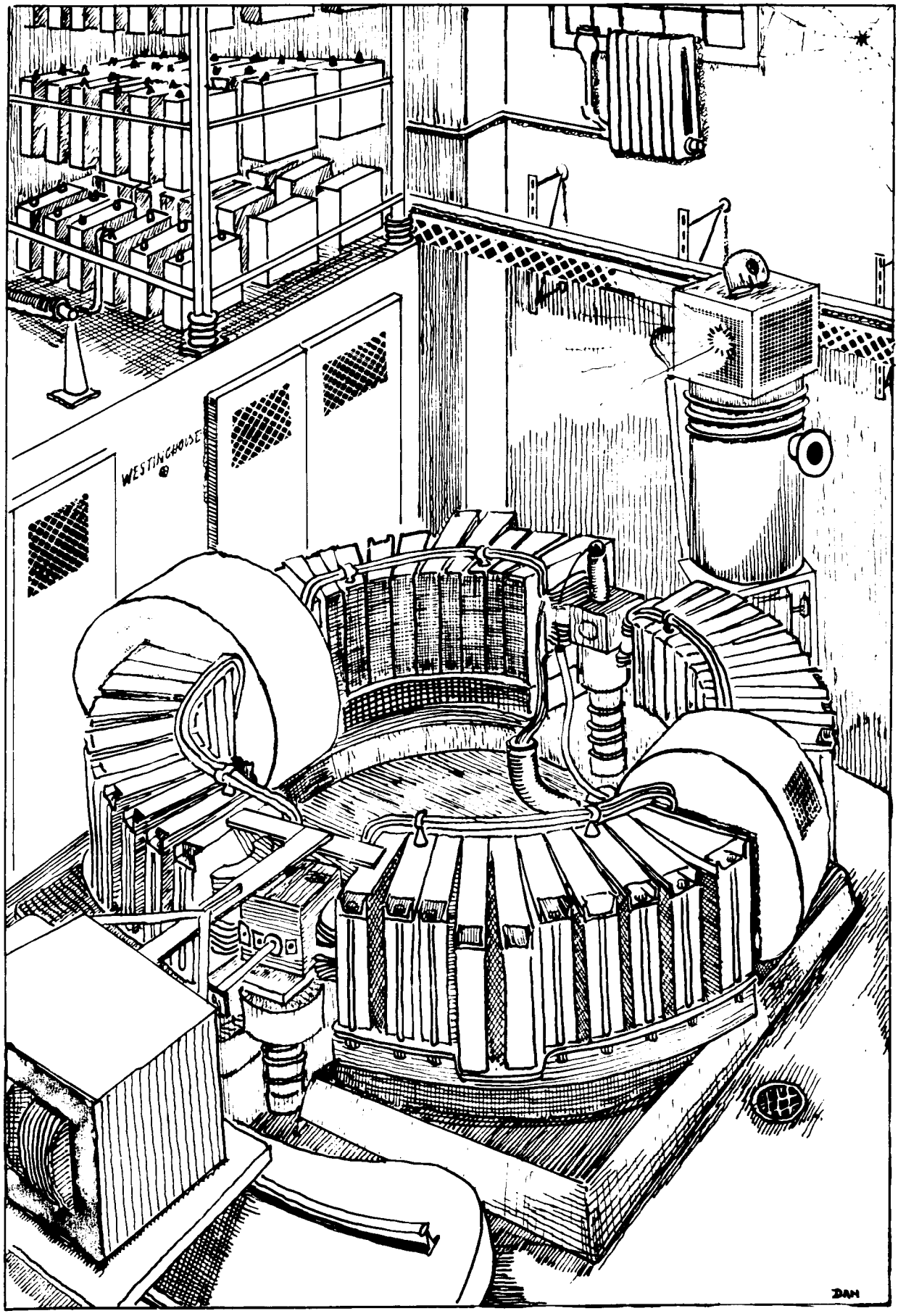

WESTINGHOUSE
DAN

A 60 MEV ELECTRON SCATTERING MEASUREMENT OF THE NUCLEAR RADII OF ALUMINUM, COPPER, AND TUNGSTEN

by
Daniel A. Nagmik

A dissertation submitted in partial fulfillment
of the requirements for the degree of
Doctor of Philosophy in the
University of Michigan
1957

Doctoral Committee:

Professor Norman R. Crane, Co-Chairman
Doctor Jerome I. Fregeau, Co-Chairman
Professor Kenneth M. Case
Associate Professor Paul V.C. Hough
Professor Lloyd D. Armbrille

ACKNOWLEDGMENTS

The author wishes to express his appreciation to the members of his committee for their interest in this work. The author is particularly indebted to Dr. J.H. Fregeau for his assistance in the interpretation of the experimental data and for his technical advice during the writing of this work, to Professor R.W. Pidd for the several preliminary discussions on experimental procedure, to A.B. Miller for his skill in operating the synchrotron and for his assistance during the scattering experiments, and to Messrs. G. Edict, O. Haas, and H.A. Westrick for their cooperation and skill in the construction of the apparatus. The author also wishes to thank his brother, Joseph Naymik, for editing and proof reading the final copy and his wife, Anne, for her encouragement and typing assistance.

The author wishes to express his appreciation to the U.S. Atomic Energy Commission for support of this work under Contract AT(11-1)-150.

TABLE OF CONTENTS

Page

ACKNOWLEDGMENTS ii

LIST OF TABLES v

LIST OF FIGURES vi

Chapter

I. INTRODUCTION 1

Historical Background

The Present Experiment

Results

II. EXPERIMENTAL APPARATUS AND PROCEDURE 8

Experimental Apparatus

Synchrotron
Collimating Slits
Momentum Analyzer
Scattered Electron Vacuum Chamber
Data Recording System
Gated Timing Marker Counter

Experimental Procedure

Analyzer Magnet Calibration
Slit Alignment
Measurement of Scattering Angles
Determination of Analyzer and Counter Response
Selection of Beam Energy
Raw Data

III. CORRECTIONS TO EXPERIMENTAL DATA 44

Counting Losses

The Radiation Loss

Multiple Scattering

TABLE OF CONTENTS-Continued

Chapter Page

Double Scattering

Geometric Corrections

Energy Loss from Nuclear Recoil

IV. DATA PROCESSING OF EXPERIMENTAL RESULTS 56

Introduction

Discussion of Results from IBM 650 Digital Computer Calculations

Comparison of Experimental Data to Theoretical Calculation

Statistical Analysis

Conclusion

BIBLIOGRAPHY 79

LIST OF TABLES

Table		Page
1.	Measurements of Beam Energy	39
2.	Unprocessed Experimental Data (Group I)	40
3.	Unprocessed Experimental Data (Group II)	41
4.	Momentum Spectra for Aluminum Taken at Three Scattering Angles	42
5.	Multiple Scattering Calculations	48
6.	Comparison of Results of Present Calculation with Results of Glassgold for Z = 74 and kR_h (Homogeneous Model) = 2.0	60
7.	Phase Shifts for Z = 74 and kR_h = 2.0 (Homogeneous Model)	60
8.	Phase Shifts for Z = 79 and kR_h = 4.0 (Homogeneous Model)	61
9.	Tungsten, Copper, and Aluminum Scattering Cross Sections for Homogeneous Model (Normalized)	64
10.	Uncorrected and Normalized Experimental Counting Rates (Counts per Monitor Count)	64
11.	Uncorrected and Normalized Deviations To Experimental Counting Rates (Counts per Monitor Count)	65
12.	Values of r_o for Tungsten, Copper, and Aluminum	65
13.	Tungsten, Copper, and Aluminum Scattering Cross Sections for Shell Model (Normalized)	74
14.	Values of the r-Statistic for Homogeneous Model	76

LIST OF FIGURES

Figure		Page
1.	Scattering Chamber	9
2.	Floor Plan of Synchrotron and Electron Detection Systems	11
3.	Photograph of Momentum Analyzer Magnet and Cerenkov Counter	15
4.	Sketch of Momentum Analyzer Magnet, Scattered Electron Chamber, Front Slit, and Cerenkov Counter	17
5.	Momentum Spectrum for Aluminum at Scattering Angle of 67° and Energy of 60.6 Mev	18
6.	Systems Schematic of Detection Equipment (Electronics)	19
7.	Cerenkov Counter and Counter Barrel	20
8.	Photomultiplier Electrical Connections and Cathode Follower Preamplifier	23
9.	Two Channel Electronic Gate Circuit	25
10.	Electronic Time Interval Counter	28
11.	Automatic Reset for Time Interval Counter	29
12.	Systems Schematic for Time Interval Counter.	30
13.	Calibration Curve for Analyzer Magnet	32
14.	Integral Pulse Height Discrimination Curve	36
15.	Histogram of Random Counting	37
16.	Normalized Momentum Spectra for Scattering Angles of 52°, 76.25°, 90°, and 103°	43
17.	Double Scattering in the Target Wire	49
18.	Geometric Correction to Single Scattering	53
19.	Theoretical Scattering Cross Sections for Z = 74, $kR_n = 2.0$	62

LIST OF FIGURES-Continued

Figure		Page
20.	Experimental Points and Theoretical Curves for Tungsten (Homogeneous Model)	66
21.	Experimental Points and Theoretical Curves for Copper (Homogeneous Model)	67
22.	Experimental Points and Theoretical Curves for Aluminum (Homogeneous Model)	68
23.	Least Square Fit of Experimental Data (Homogeneous Model)	69
24.	Experimental Points and Theoretical Curve for Tungsten (Shell Model)	71
25.	Experimental Points and Theoretical Curve for Copper (Shell Model)	72
26.	Experimental Points and Theoretical Curve for Aluminum (Shell Model)	73

CHAPTER I

INTRODUCTION

Historical Background

Advances in electron scattering experiments as a technique for measuring nuclear sizes and investigating nuclear structure can be marked by the development of the high energy accelerators. After Rutherford (1) experimentally verified the Rutherford scattering law which was derived from principles of classical mechanics, it was not until 1951 when Lyman, Hanson, and Scott (2) did scattering experiments using 15.7 mev electrons from a betatron that deviations from the Mott scattering formula were noted. The Mott formula is derived from principles of quantum mechanics and is essentially the Rutherford formula corrected for the effect of spin and relativistic energies of the scattering particle. The development of scattering experiments as a probe for determining nuclear size was slow during the period 1930-1950 for two reasons: (1) a source of high energy electrons with high incident flux was lacking, and (2) inherent experimental difficulties in cloud chamber experiments resulted in conflicting reports from various research groups.

A number of authors (3, 4, 5, 6, 7) published papers which indicated that the potential in a scattering problem had to be, not Coulomb, but one due to a distribution of charge. This suggested that the size of the nucleus would account for the scattering patterns obtained from 15.7 mev electrons striking a gold target in the Lyman,

Hanson, and Scott experiment. Thus, the same effect enters in electron scattering as it had in light scattering and X-ray diffraction; that is, when the wave-length of the scattering particle becomes the same order of magnitude as the dimensions of the scatterer, deviations from the opposite case (wave-length greater than the dimensions of the scatterer) are to be expected.

The work of Lyman, Hanson, and Scott was compared to the calculations done by Elton (5) and Acheson (3). This was an exact phase shift calculation which required only one phase shift for energies of order 20 mev. The calculation assumed that the electrostatic potential was due to a homogeneous distribution of nuclear charge. The experimental data was a measure of the ratio of the actual scattering cross section to the Mott scattering cross section. This ratio was determined for aluminum, copper, silver, and gold target nuclei; only for aluminum was the ratio one. This seems reasonable since the radius of the aluminum nucleus is smaller than the reduced wave-length of the scattering electron, and, therefore, finite size effects would not enter into this situation. The experiment of Lyman et al concluded that a nuclear charge was distributed uniformly over a volume whose radius is $r_o = 1.45 \times 10^{-13}$ cm (1.45 fermis). This conclusion was obtained by fitting the ratio of experimental cross section to the Coulomb scattering cross section as a function of scattering angle ($\theta = 30^o(30^o)150^o$) to the theoretical curves furnished by Elton (5) and Acheson (3); the parameter for this family of curves is kR_h, where k is the wave number of the electron being scattered and R_h is the radius of the nuclear charge distribution. The subscript h denotes that the assumed charge distribution is a homogeneous one. Elton indicates that $R = r_o A^{1/3}$ cm, where

$r_o = e^2/mc^2$ is the Compton wave-length of the electron which is equal to 2.817×10^{-13} cm.

In 1953 Pidd, Hammer, and Raka (8) extended the investigation of nuclear sizes when they succeeded in producing a 40 mev beam of electrons from the University of Michigan synchrotron. Beam extraction was not required in this experiment as the scattering chamber was made a part of the synchrotron. The Hammer-Raka apparatus included two detection systems since monitoring the incident beam flux with a Faraday chamber was impractical without beam extraction. One detection system placed inside the synchrotron racetrack at a fixed angle acted as a monitor for the other detection system which recorded the electrons that were scattered at several angles by the target foil. The ratio of counts recorded by the detection system to counts recorded by the monitor system corrected for losses due to multiple scattering, geometric aperture correction, and radiative losses were plotted against five experimentally measured scattering angles and compared to a single phase shift calculation of Acheson (3). Feshbach (9) had concluded that calculations for scattering cross sections at 40 mev require only one phase shift which is independent of the nuclear model chosen.

For the tungsten nucleus Hammer (10) found that $r_o = 1.04 \pm .07$ fermis for the homogeneous charge distribution at the two incident electron energies of 33 and 43 mev. Raka's (11) work was a measurement of scattering cross sections at 60^o relative to scattering at 90^o for electrons of incident energy 33 mev and for scattering targets of palladium, silver, cadmium, indium, tin, antimony, and tellurium. For these conditions he concluded that there should be no irregularities greater than one percent in the, so-called, $A^{1/3}$ law (volume proportional to

the number of nucleons).

Hofstadter et al (12, 13) have conducted a comprehensive study of nuclear sizes and structure with the electron beam produced by the University of Stanford linear accelerator. Experiments have been conducted at beam energies ranging from 125 mev to 550 mev. Elastic scattering experiments at 183 mev using Ca, V, Co, In, Sb, Hf, Ta, W, Au, Bi, Th, and U target nuclei have been made by Hahn, Ravenhall, and Hofstadter (14). The experimental data were fitted to three test models of proton charge distributions. These models contain two radial parameters. One parameter essentially determines the nuclear diameter and the other determines the "skin thickness" of the nucleus. The purpose of this investigation was to study how these two parameters varied over the range of nuclei from Ca to Bi. The diameter parameter was measured with two percent accuracy, while the "skin thickness" parameter was measured with ten percent accuracy. Similar elastic scattering measurements at 153 mev, using gold, indium, and bismuth targets, were also made by Hahn et al (14). One of the results from these experiments indicates that the non-spherical nuclei (Hf, Ta, W, Th, and U) have diffraction dips in the scattering cross sections which are smoothed out. These dips have been analyzed by Downs, Ravenhall, and Yennie (15) as evidence for quadrupole distortions.

In order to obtain information about the 0-2 transitions between ground and first excited states, inelastic scattering from the even-even nuclei ${}_{12}Mg^{24}$, ${}_{14}Si^{28}$, ${}_{16}S^{32}$, ${}_{18}A^{40}$, and ${}_{38}Sr^{88}$ has been studied by Helm (16). At the same time elastic scattering data for these nuclei were also obtained, and the radial parameters determined for each of these nuclei. Inelastic and elastic scattering of 187 mev

electrons from C^{12} has also been reported by Fregeau and Hofstadter (17) and, in greater detail, by Fregeau (18).

The data from the elastic scattering of electrons with energies 100, 188, 210, and 236 mev by hydrogen gas at high pressure (2000 psi) have been reported by McAllister and Hofstadter (19). Results of these experiments indicated departures from Rosenbluth's (20) point charge and point magnetic moment calculations. Subsequent experiments between electron energies of 200 mev and 550 mev by Chambers and Hofstadter (21) indicate that the experimental data fits theoretical calculations in which the root mean square radii for both the proton's charge and the magnetic moment distributions are equal to 0.77 ± 0.1 fermis. In fact, the elastic scattering of electrons from deuterons produced data which can be fitted with form factor calculations when a finite proton having a spread out charge and a spread out magnetic moment is assumed as a model of the proton within the deuteron. These data were obtained by McIntyre and Hofstadter (22) at 192 mev and by McIntyre (23) at 188 and 480 mev.

The Present Experiment

The present experimental work is centered around the University of Michigan synchrotron, which is the source of 60 mev electrons that are used as incident particles to be scattered from an aluminum, copper, and tungsten target wire. Although the machine is capable of producing an 88 mev beam, it was decided to use a 60 mev beam in this experiment. At this energy counting rate measurements at all scattering angles give statistical errors whose magnitudes are approximately the same as those errors resulting from a measurement of the beam energy. The combined effect of counting rate measurements, however, causes any error in the

constant of proportionality, r_o, in the $A^{1/3}$ law to be determined principally by the error made in measuring the energy of the incident electron beam.

Although r_o has been measured for a large number of target nuclei and for several energies, measurements of this kind have not been made for aluminum and copper at energies above 45 mev. Measurements of r_o for tungsten at 60 mev have been made by Pidd and Hammer (24) who used 5 scattering angles and quoted an experimental accuracy of 10 percent for r_o.

The present experiment is a measurement of the total number of electrons scattered at each of seven angles relative to the number of electrons scattered at a fixed angle. This measurement is proportional to some particular theoretical scattering cross section which is calculated from Dirac theory for an assumed model of proton charge distribution. The scattering cross section is a function of the scattering angle and a parameter kR, where k is the wave number of the electron and R is proportional to r_o. By shape fitting the experimental data to these curves one can select a particular value for kR which then determines a value for r_o, the number which is quoted in any statement about the $A^{1/3}$ law. The theoretical calculations for the shell distribution and the homogeneous distribution of nuclear charge are compared to the data of this experiment. Such a comparison will determine whether or not the scattering patterns at 60 mev depend upon the model of the nucleus that is chosen.

Results

The average of two independent measurements of the synchrotron beam energy is 60.6 mev, and these measurements show that the error in measuring energy is less than 5 percent. If one takes the upper limit

of this error, then the errors in the values of r_o for tungsten, copper, and aluminum are at least of the order of 5 percent. From this experiment it can be concluded, by assuming a homogeneous model for the nuclear charge distribution, that the values of r_o for tungsten, copper, and aluminum are 1.14 ± .06, 1.15 ± .06, and 1.41 ± .07 fermis, respectively.

Comparison of experimental results with the theoretical calculations shows that the experimental data for tungsten can be fitted better to the homogeneous model calculations than to the shell model calculations. However, either the homogeneous or the shell model calculations can be used to fit the experimental data of aluminum and copper. This is true because the scattering cross section at 60 mev for the two models differs by a few percent at each angle and because the errors in counting rate measurements of this type are of the order of 5 percent.

CHAPTER II

EXPERIMENTAL APPARATUS AND PROCEDURE

Sixty mev electrons from the synchrotron are made to collide with a scattering target located in a scattering chamber. These collisions form a scattering pattern whose characteristics are investigated by means of two detector systems; one, called the monitor, records a number which is proportional to the total electron incident beam flux, and the other, called the detector, records a number which is proportional to the elastically scattered beam flux. The detector system can be placed in any one of seven scattering angles.

The collisions forming the scattering pattern are caused when the acceleration process of the synchrotron ceases, and as the magnet guide field continues to increase, the equilibrium orbit of the electrons decreases to a smaller radius at which a target wire has been placed. The target wire is mounted vertically in a pinwheel which is fastened inside one of the four straight sections of the synchrotron. This pinwheel can be rotated by remote control so that targets can be changed while the machine is in operation. Figure 1 is a view showing the inside of the scattering chamber. The cover plate for this chamber (not shown in the figure) has seven valves which lie in a horizontal plane when the cover plate is in position. Each valve is made so that a slit housing can be clamped to it. The slit housing contains the front slit which admits the scattered beam into the detector system;

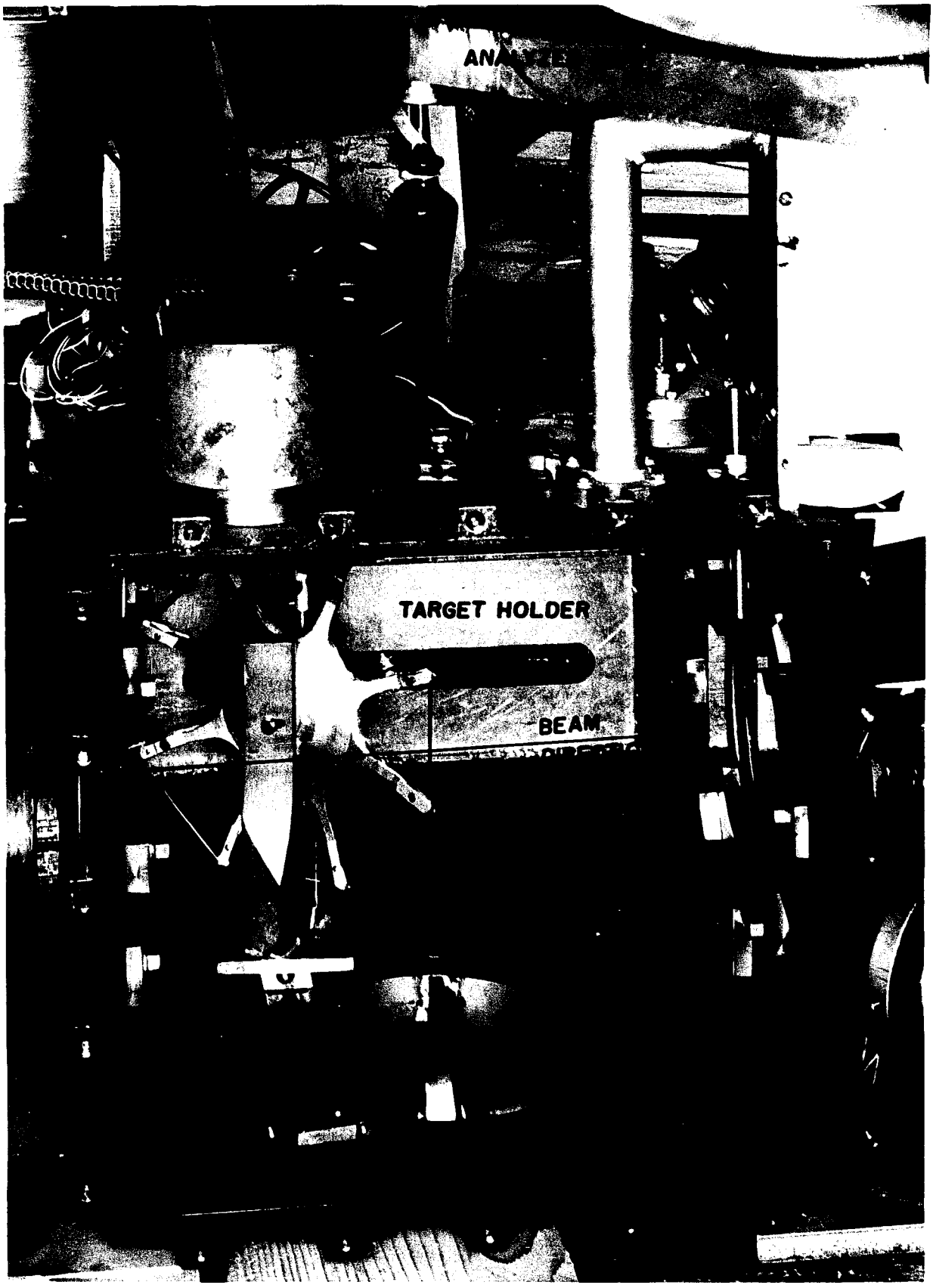


Figure 1. Scattering Chamber

the other end of the slit housing is clamped to a scattered electron chamber, a brass box located between the pole faces of an analyzer magnet. When the valve is opened, a 3/4-inch port hole enables the slit housing and the scattered electron chamber to be evacuated along with the synchrotron vacuum chamber.

The scattered electron vacuum chamber contains a 5 mil aluminum window outside of which is a Cerenkov counter. This counter detects the passage of electrons through the solid angle defined by the front and back collimating slits. The back slit is located inside the Cerenkov counter housing.

The monitor system is located inside the synchrotron; it detects the passage of charged particles coming from the target through a solid angle defined by a collimating slit. Unlike the detector unit the monitor is a stationary system. Figure 2 shows a floor plan of the physical arrangement of the apparatus in the synchrotron room.

The scattering patterns from aluminum, copper, and tungsten wire targets of thicknesses 20 mils, 20 mils, and 5 mils, respectively, were investigated in this experiment.

Experimental Apparatus

Synchrotron

The University of Michigan synchrotron contains a straight section that provides a region whose magnetic field is negligibly small compared to the synchrotron guide field. Within this region electron scattering experiments can be conducted. This eliminates the problem of extracting the beam from the synchrotron for such scattering experiments. The scattering chamber, a 10-inch cubically shaped iron box, then, is one of the straight sections of the synchrotron. The box

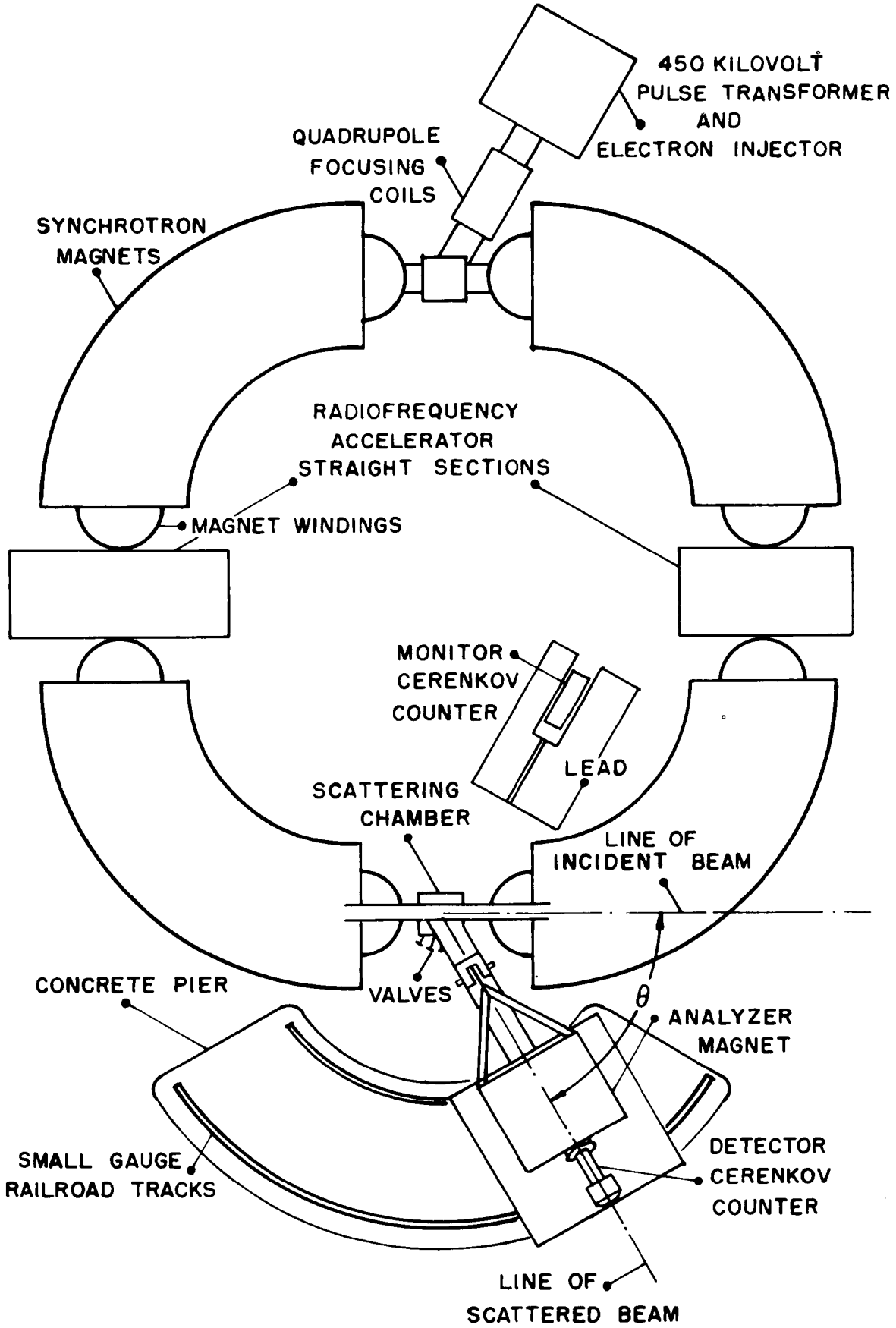


Figure 2. Floor Plan of Synchrotron and Electron Detection Systems.

magnetically shields the target region from the fringe field of the synchrotron magnets. Measurements indicate that the field at the target position is 4 gauss when the magnet guide field at equilibrium orbit is 2884.5 gauss (25). The acceleration process takes place by synchronization of two radio-frequency oscillators, each one located at a straight section. The fourth, and last, straight section is used for injection of a 450 kv electron beam. This machine is capable of producing an 83 mev electron beam containing 10^9 electrons per pulse at a pulse rate of 20 per second. Energy resolution is of order 1 percent (10). Stability at any design energy is limited by fluctuation of the 220-three phase line voltage that provides power to the 20 cycle magnet oscillator. The frontispiece depicts the synchrotron.

Collimating Slits

The front collimating slit for the detector system is a lead cylinder that is 1 inch in diameter and 4 inches long with a hole, one-fourth of an inch in diameter, bored through it. A slit housing, which is a 1-inch hollow brass tube 14 inches long, rigidly suspended from the analyzer pivot yoke, holds the collimating slit in position. The distance between the target end of the collimating slit and target is 13 inches. The housing can be unclamped from its suspension brackets so that various sizes of slits can be inserted into the housing for test purposes. The suspension brackets are rigid in order to preserve the original alignment of the slit housing and the slit contained within it.

The back collimating slit for the detector system is a lead cylinder 2 inches long and 3 inches in diameter; it has a 1-inch diameter x 2-inch hole bored through its axis. This collimator is clamped to the

front end of the Cerenkov detector counter barrel. The counter barrel is rigidly clamped to the analyzer magnet so that the collimator hangs outside the 5 mil aluminum window which covers the exit port of the scattered electron chamber.

There is only one collimating slit for the monitor detector system. It is a lead cylinder 2 inches in diameter and 8 inches long with a one-eighth of an inch diameter x 8-inch hole bored through it. The end nearest the target is 24 inches from the target, and the end nearest the monitor is 8 inches from the monitor. Optical alignment is used to place the target, the collimator, and the monitor on the same line; this line makes an angle of 54 degrees with the incident beam direction.

Momentum Analyzer

A 20-inch x 26-inch x 28½-inch, one-and-a-half-ton H-Magnet is used for a momentum analyzer. It was originally designed to deflect a 300 mev beam of electrons through an angle of 30 degrees. The particle trajectory radius of curvature is 40 inches. The magnet coils are water cooled and are made of 1/8-inch copper tubing which is wrapped in fiber glass. The pole faces were designed to give partial focusing in a plane perpendicular to the field between the pole faces.

The magnet is placed so that the magnetic field lines between its pole faces are parallel to the median plane of the synchrotron—the plane which contains the equilibrium orbit of the accelerating electrons. This orientation for the analyzer then places the detector Cerenkov counter 12 inches above the median plane. It was necessary to locate the counter out of the median plane because tests showed that the background counting rates with the detector in the median plane

were excessively high, particularly at the larger scattering angles.

The analyzer sits on four ball bearings which are imbedded in a platform; under this platform are four ball bearing wheels that roll on small gauge railroad tracks. This arrangement prevents the magnet from straining the pivot around which it moves.

A yoke is bolted to an angle iron which is fastened to the front surface of the analyzer. An adjustment screw enables the magnet to be pivoted around a point where the yoke is bolted to the angle iron. This adjustment is used only for the initial alignment of the magnet so that its focal point can be placed at the target wire. The other end of the yoke swings around a ball bearing pivot which can be adjusted so that the magnet itself can be made to swing along a circular path whose center lies on a vertical line through the target wire. Figure 3 shows a photograph of the analyzer. All the lead shielding has been removed so that the front slit housing and its suspension bracket (left side of photograph) can be seen. The Cerenkov counter barrel can be seen in the upper right side of this photograph.

The current in the analyzer magnet is regulated by a 2B23 vacuum tube suspended in an air core solenoid electrically connected in series with the magnet coils. Fluctuation of solenoid current causes the plate current of the 2B23 vacuum tube to fluctuate also; the output of this tube then acts as input to a magnet current regulator of conventional design. This arrangement regulates the current to better than 0.1 percent. An R-C filter in the magnet current circuit attenuates the higher harmonics from the output of the 10 kva D.C. generator used to provide the D.C. field current for the analyzer magnet.

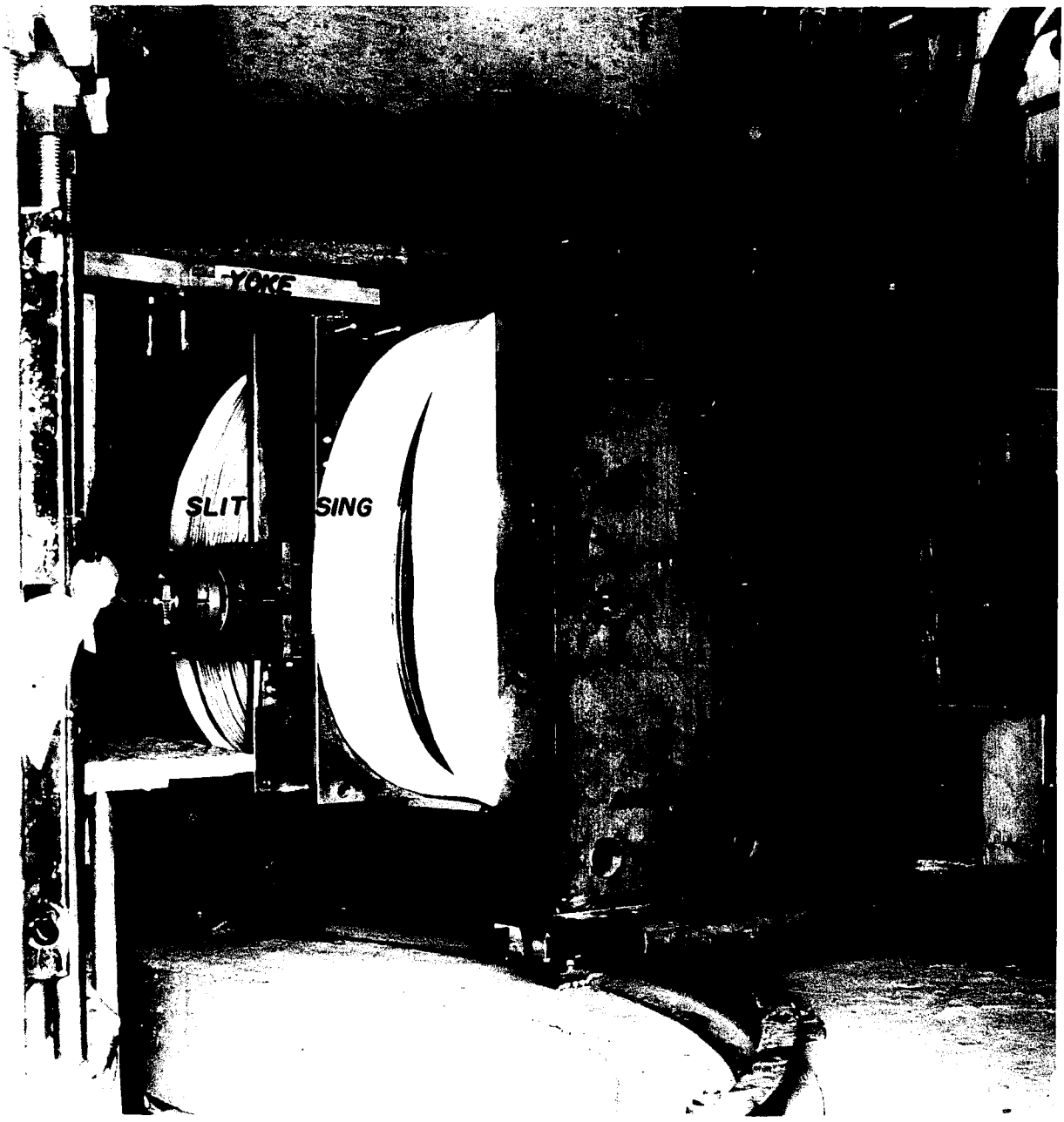


Figure 3. Photograph of Momentum Analyzer Magnet and Cerenkov Counter

Scattered Electron Vacuum Chamber

This chamber is a brass box through which the scattered beam passes after being admitted through the front collimating slit of the detector counting system. The orientation of the box with the front collimating slits, back collimating slits, and the detector counter are depicted in Figure 4, which is a sketch of the components shown in the photograph of Figure 3.

The box is evacuated in order to minimize multiple and plural scattering of the electrons, and thereby increase the efficiency of detection. Multiple scattering in the aluminum window just in front of the Cerenkov detector counter does not affect counter efficiency.

The box was constructed with a somewhat triangular shape in order to improve the character of the momentum spectrum for the analyzer current settings in the range of 10 to 14 amperes. The dotted curve in Figure 5 shows the appearance of the momentum spectrum taken when a, now obsolete, scattered electron chamber, shaped in a manner indicated by the dotted line in Figure 4, was installed in the detector system.

Data Recording System

A block diagram of the data recording system is shown in Figure 6. In the following paragraphs details of each component of this system are given. Except for the two Cerenkov counters and their cathode follower circuits, all components of the data recording system are located in the data room next to the synchrotron control room.

1. Cerenkov counters. Figure 7 shows a photograph of the detector Cerenkov counter. There are two parts to this counter; a lucite radiator and a 6363-type Dumont photomultiplier.* The lucite radiator has cylindrical symmetry. It is a truncated cone four inches

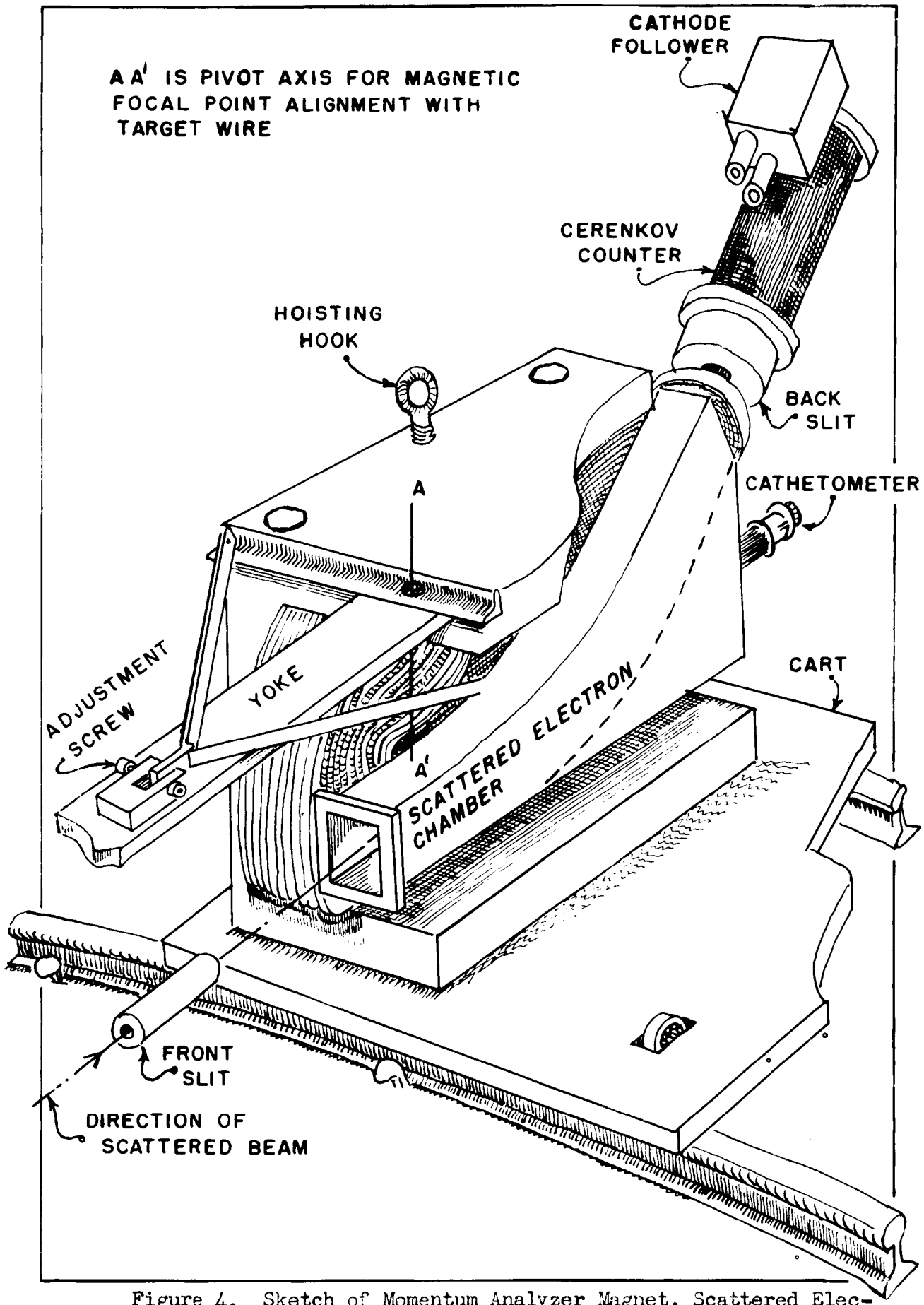


Figure 4. Sketch of Momentum Analyzer Magnet, Scattered Electron Chamber, Front Slit, and Cerenkov Counter.

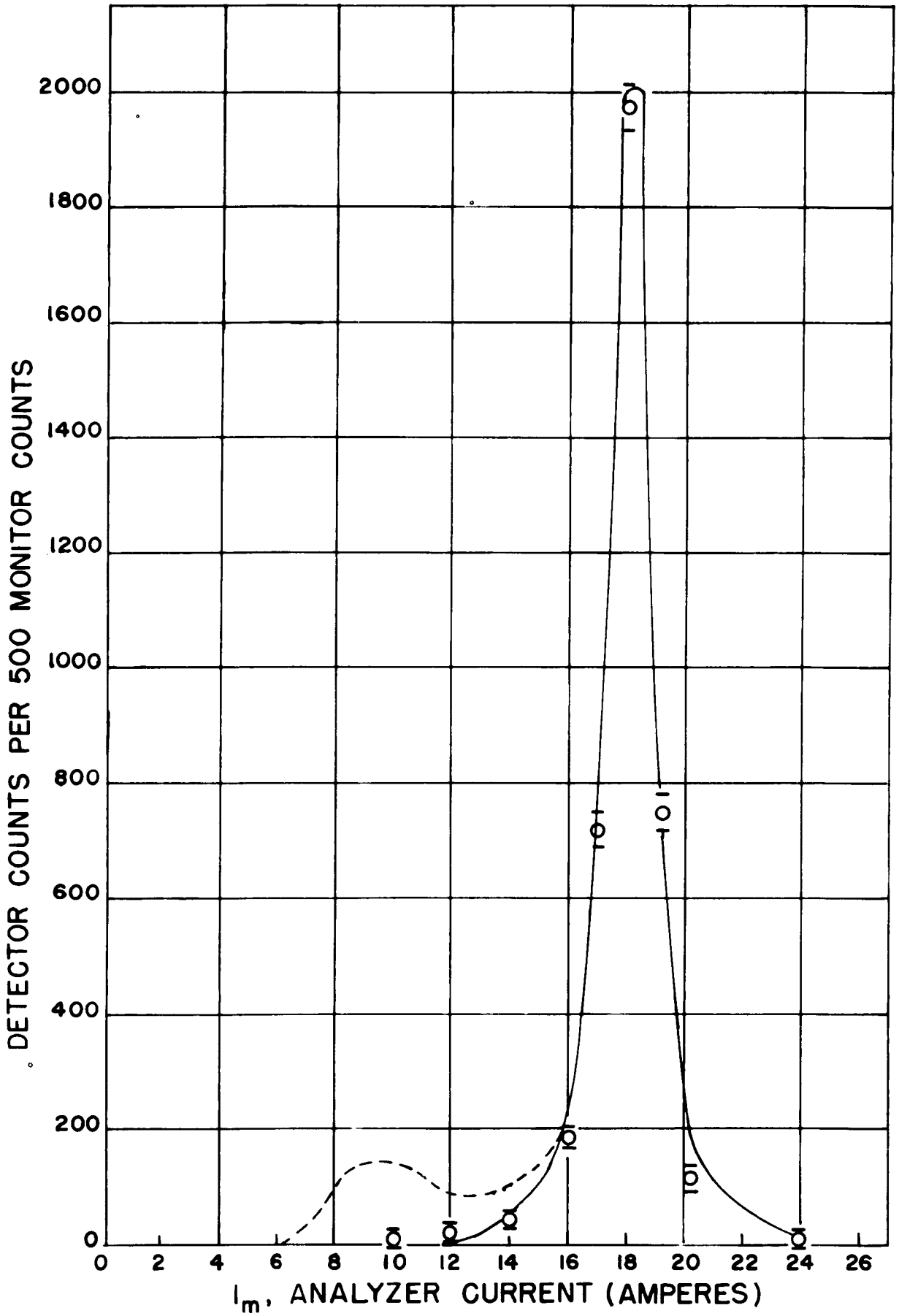


Figure 5. Momentum Spectrum for Aluminum at Scattering Angle of 67° and Energy of 60.6 Mev.

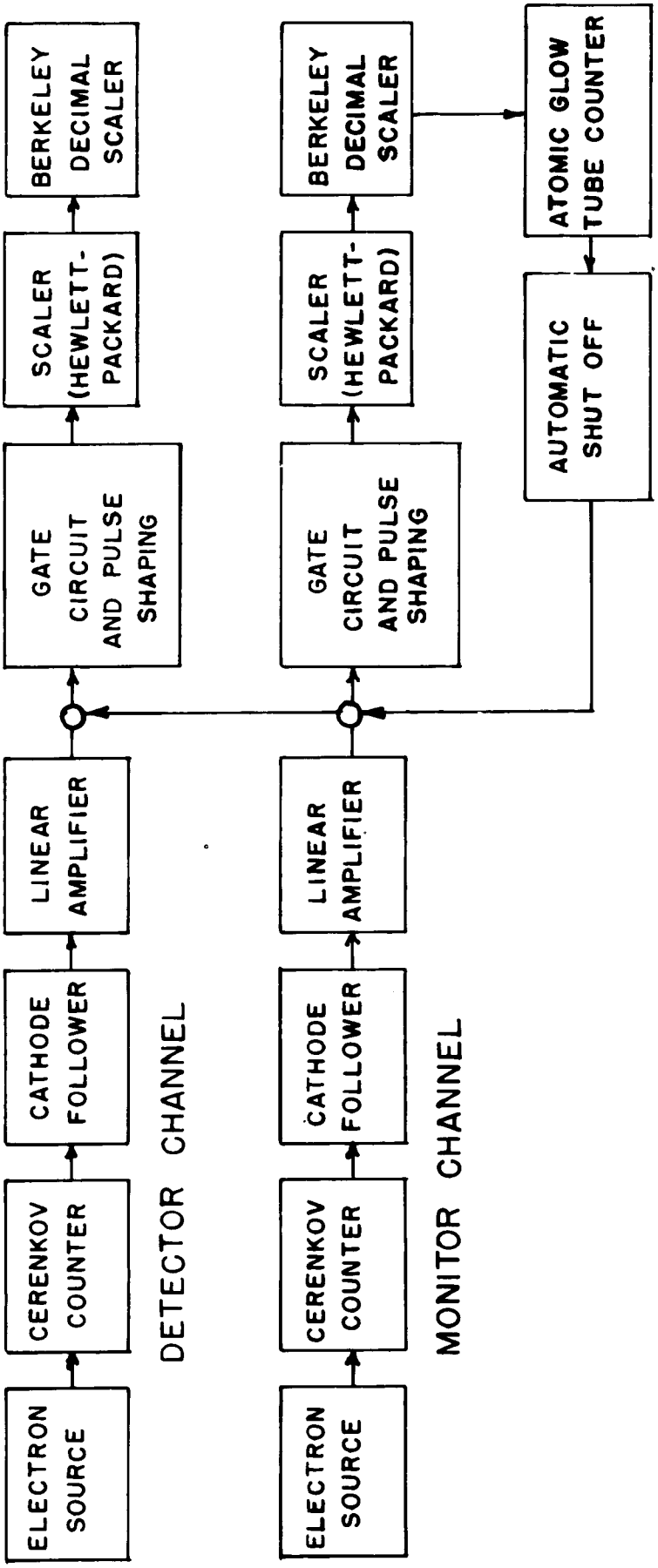


Figure 6.° Systems Schematic of Detection Equipment (Electronics).

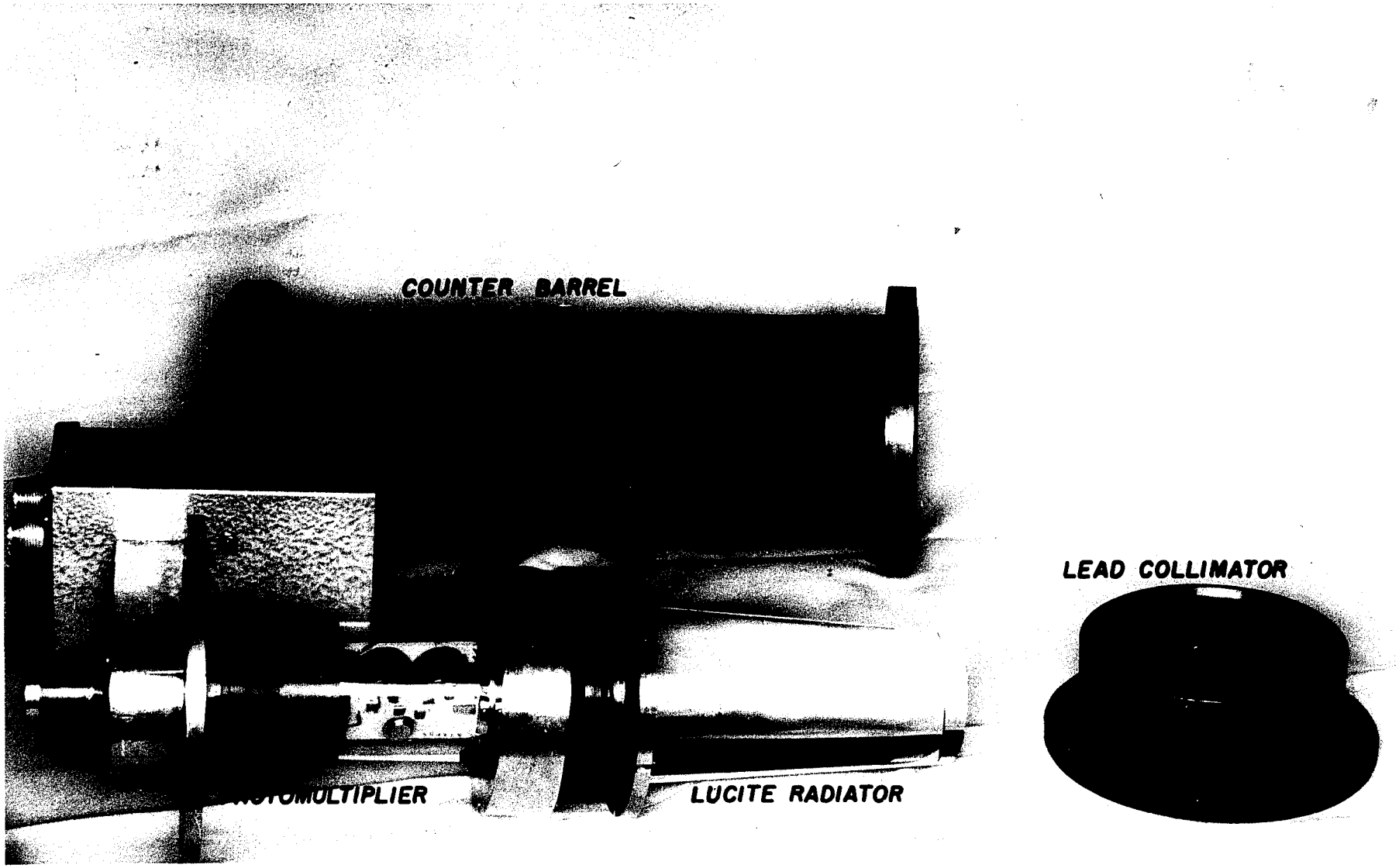


Figure 7. Cerenkov Counter and Counter Barrel

long, having a front face 2 inches in diameter and a back face 3 inches in diameter. This cone is clamped to the end window of the photomultiplier tube by a dural aluminum ring which is tapered inside so that the cone fits snugly in the ring. Varnished cambric is wrapped around and taped to the phototube envelope; Scotchcast (Minnesota Mining and Manufacturing Company) is used to glue the varnished cambric to the dural aluminum ring. This arrangement forms a reservoir for holding silicone oil with a viscosity of 100,000 centipoise. The oil, therefore, can be contained in the interface between the lucite radiator and phototube improving the transmission of Cerenkov light from the lucite to the photocathode surface.

The two components of the Cerenkov counter are sealed in a light-tight chamber made of galvanized iron pipe. A solid brass plate is clamped to a flange that has been welded to the end of the galvanized iron pipe. This flange contains a groove in which a 1/8-inch x 4-inch diameter rubber "O" ring is placed, thereby ensuring a light-tight seal. A bracket is bolted to this brass plate; it supports a chassis that contains cathode follower circuit components. The other end of the galvanized iron pipe also has a flange welded to it; it also has a groove with a 1/8-inch x 4-inch diameter "O" ring in it. This end has a 5 mil aluminum foil which has been placed against the "O" ring and clamped into position by a $\frac{1}{4}$-inch-thick dural aluminum ring with an outside diameter of $4\frac{1}{2}$ inches and an inside diameter of 3 inches. The detector counter is oriented in this galvanized iron barrel so that the lucite radiator is nearest the aluminum foil. The aluminum foil protects the photocathode surface from extraneous light and, at the same time, acts as a window through which charged particles may enter with

small probability of plural or multiple scattering.

Since the unit sits in the fringe magnetic field of the analyzer magnet, the inside of the counter barrel is lined alternately with sheets of aluminum foil and hypersil in order to further magnetically shield the photomultiplier. Five sheets of aluminum foil and five sheets of hypersil are alternatingly used.

Figure 8 shows a diagram of the electrical connections made for the photomultiplier tube and the manner in which it is coupled to a cathode follower circuit. The output of the cathode follower (output impedance of 90 ohms) is a 100 ohm coaxial cable 195 feet long that leads into the data room. The output of the cathode follower is amplified by a linear amplifier (Atomic Instrument Company, Model 204B) having a rise time of 0.2 microsecond.

A Cerenkov counter is used in this experiment in order to reduce background for all scattering angles. Cerenkov radiation is a characteristic property of charged particles traveling through a medium such as lucite with velocities greater than the velocity of light through this medium. Thus, a device, sensitive to Cerenkov radiation, can discriminate between high speed charged particles and neutral particles or slow charged particles. Since lucite is a poor scintillator and pair production by high energy gamma rays in 4 inches of lucite was experimentally shown to be unlikely, the background due to neutral and low energy electrons is of order one percent of the signal counting rate.

The monitor counter is constructed in a manner very similar to the detector counter. The lucite radiator, however, is a truncated cone whose front face is 1 inch in diameter and whose back face is 2 inches in diameter. The phototube for the monitor counter is an RCA-5819.

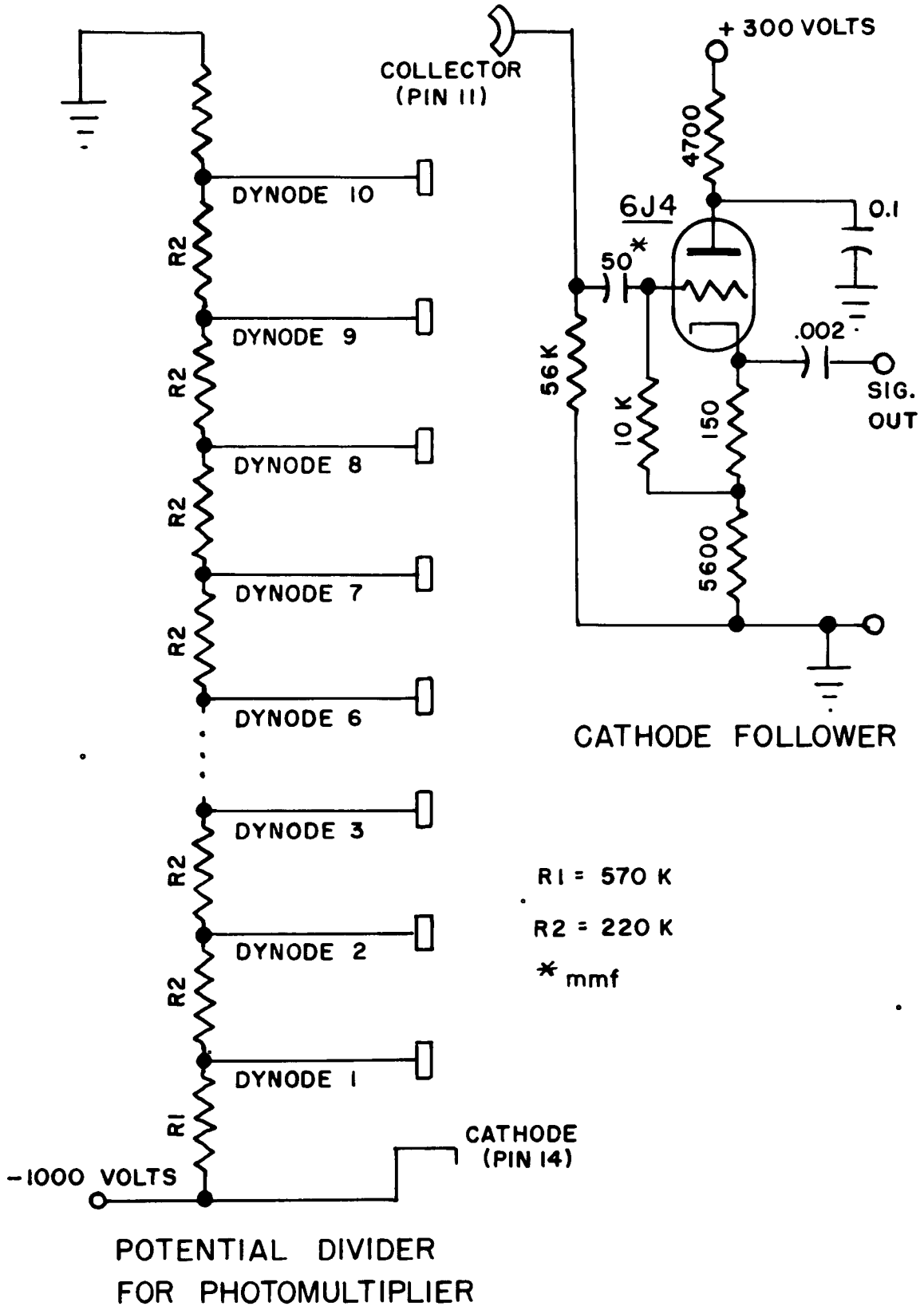


Figure 8. Photomultiplier Electrical Connections and Cathode Follower Preamplifier.

The galvanized iron counter barrel for the monitor counter has the same construction features as the detector counter, but its physical dimensions are smaller.

2. Gating circuit. The radiation that occurs in the synchrotron room between injection time and the time that the beam begins hitting the target is intense enough to cause spurious counts to be recorded through the effect of pile-up of small pulses. In order to eliminate this difficulty an electronic gate circuit is used as a time discrimination device. The circuit diagram of this unit is shown in Figure 9. It permits counts to be recorded only during the time interval, about 30 microseconds, that the electrons in the beam are hitting the target. The gate is triggered by the same pulse which turns off the radio-frequency oscillators used in accelerating the beam, and a time-delay control adjusts the gate so that it is triggered "on" when the beam is hitting the target. An oscilloscope is used for this adjustment.

3. Scalers. In order to reduce counting loss without reducing signal counting rate, Hewlett-Packard high speed (Model 510A) scalers are used for both the detector and the monitor counting. These scalers record a maximum of 100 counts. They generate a 20 volt positive pulse for every 100 counts recorded; this positive pulse can then be recorded by a slower scaler, such as a Berkeley (Model 410A) scaler which is used in recording detector counts or an Atomic Instrument Company (Industrial Glow Tube) counter which is used in recording monitor counts.

The glow tube counter circuit contains a relay which is actuated whenever the glow tube counter has recorded a pre-set number of counts. This feature is used as a "stop-count" control for both the detector and

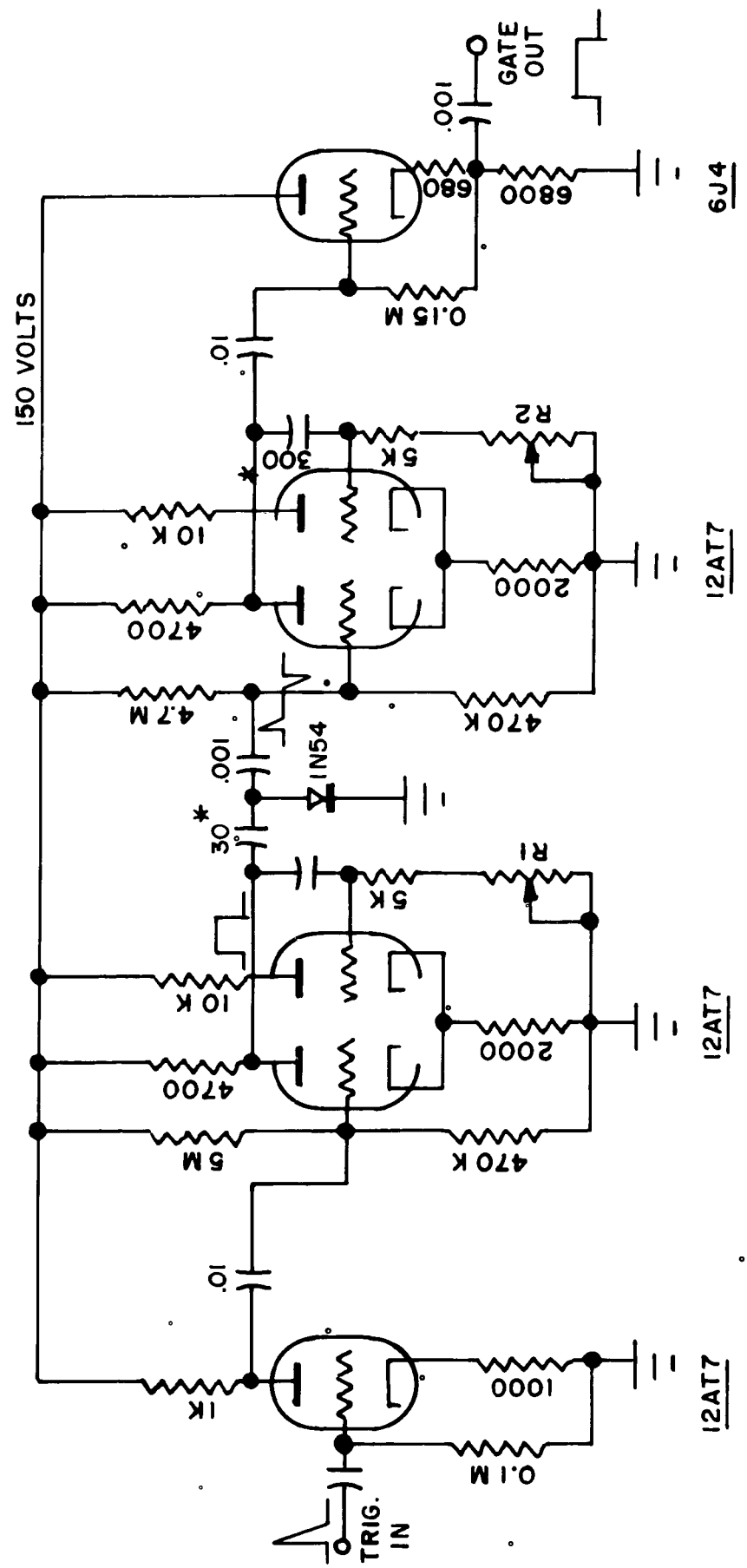


Figure 9. Two Channel Electronic Gate Circuit. (Continued on next page)

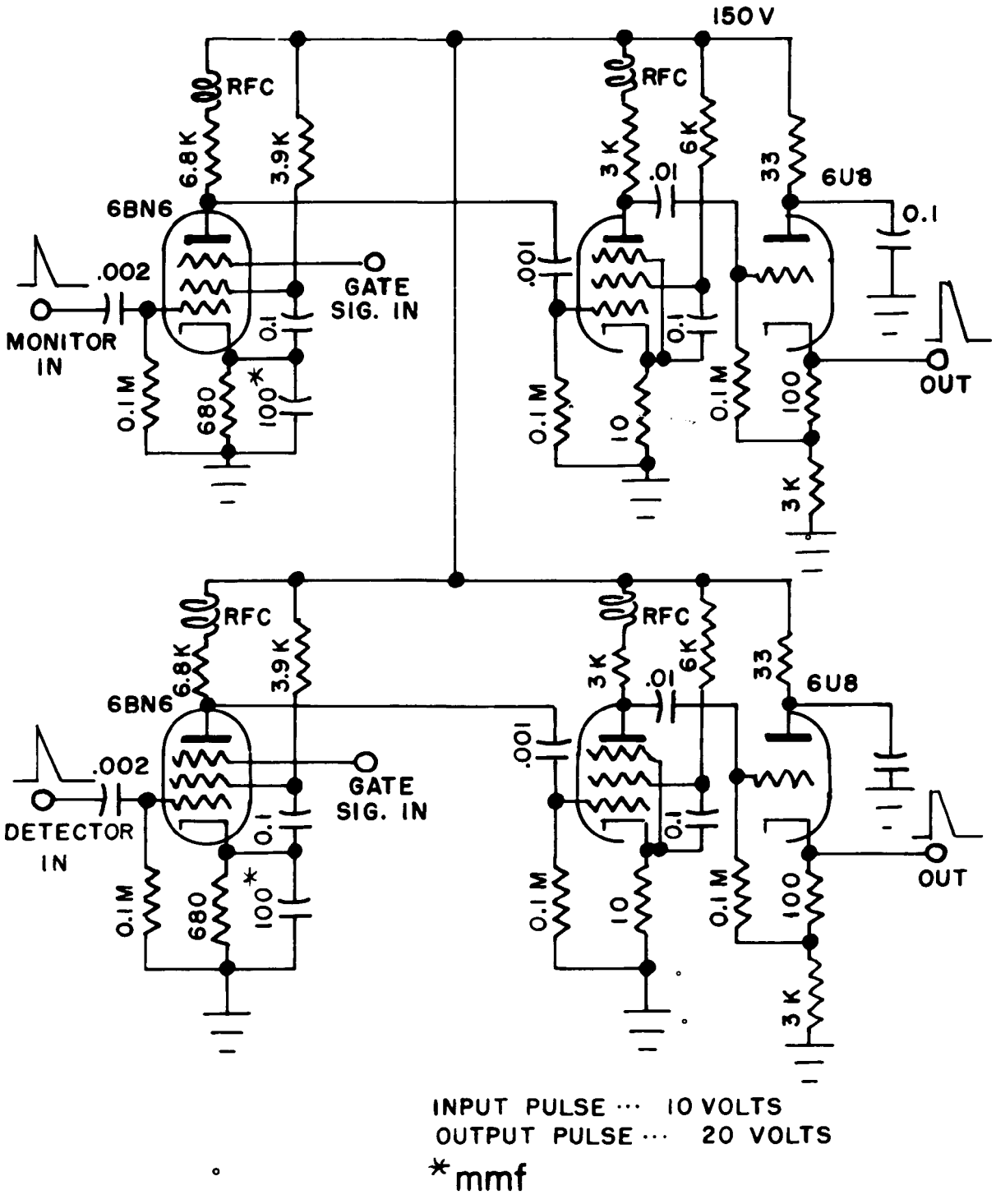


Figure 9 - (Continued)

the monitor. The "stop-count" control is a relay switch which is in series with the gate trigger source. The glow tube counter is set to record an arbitrary number of counts. When the monitor scaler detects this number, the relay actuates and, thus, prevents gate triggering. Both monitor and detector stop recording counts. The scalers also have a remote reset control.

Gated Timing Marker Counter

To determine the beam energy it is necessary to measure the peak magnetic guide field at the position of the equilibrium orbit, the total time of acceleration, the frequency of oscillation of the synchrotron guide field, and the radius of curvature of the equilibrium orbit (25). The measurement of total time of acceleration is accomplished by a circuit whose schematic is shown in Figures 10, 11, and 12. The circuit is basically a scaler which is gated so that a "t_i" (initial time instant) pulse opens the electronic gate allowing the scaler to record regularly spaced pulses with a repetition rate of 50 kilocycles per second, and a "t_f" (final time instant) pulse closes this gate in order to discontinue counts to the scaler. Thus, $t_f - t_i$ = number of pulses recorded from a 50 kilocycle generator times 20 microseconds. For time intervals measured in this experiment the accuracy was of order 1 percent.

Experimental Procedure

Analyzer Magnet Calibration

Magnet calibration is necessary in order to determine the momentum of the elastically scattered electrons. Calibration can be done by using α - particles of known energy from a radioactive material or by performing a hot wire experiment; the latter technique is used for this

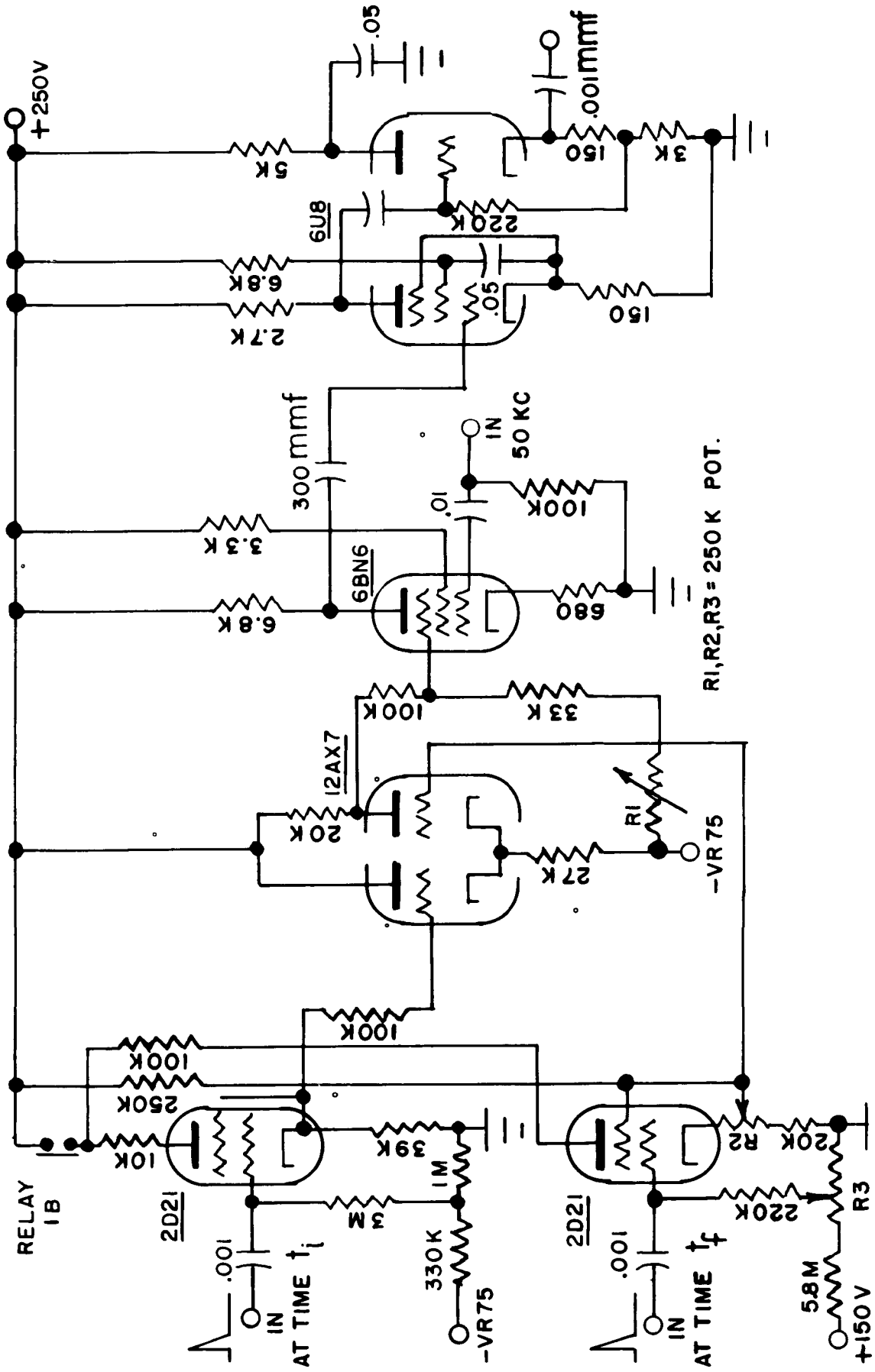
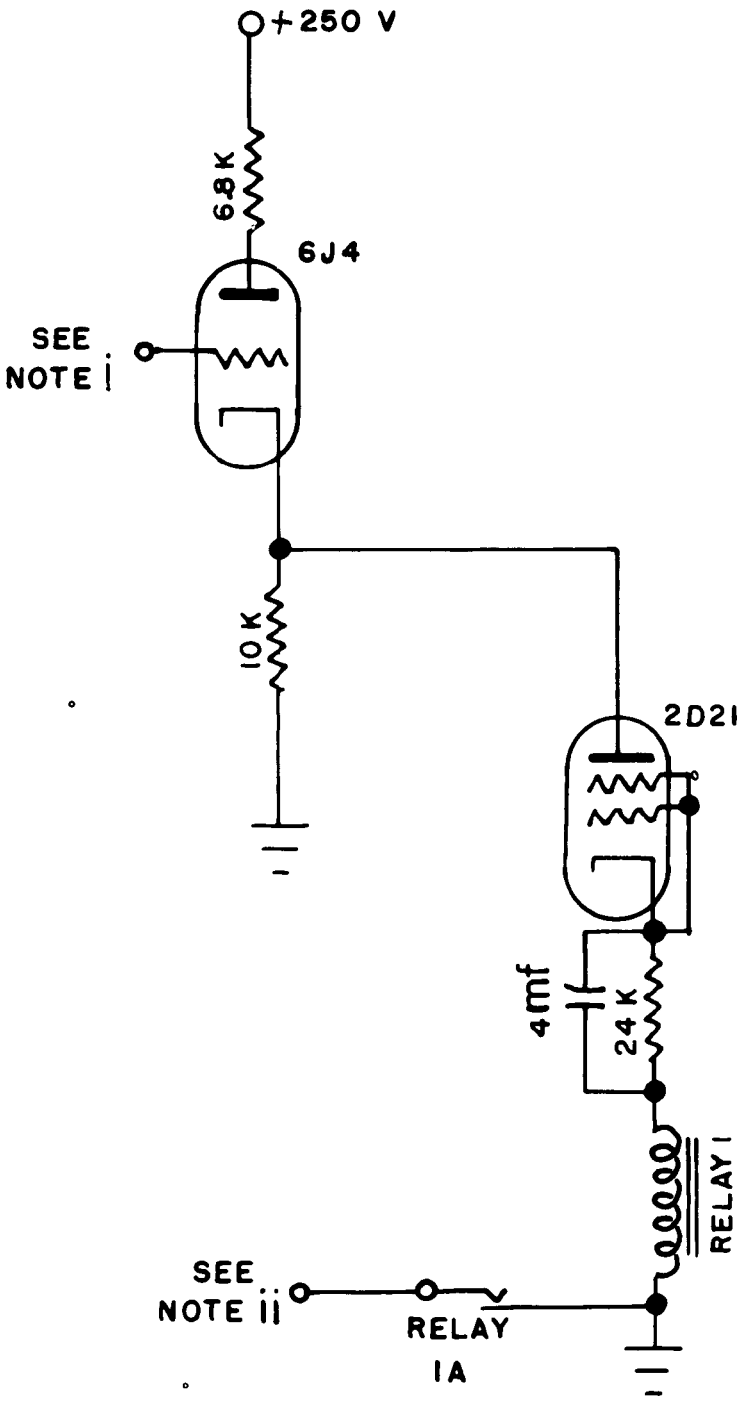


Figure 10. Electronic Time Interval Counter.



NOTE i: TO OUTPUT OF 705A SCALING UNIT. THIS GRID HAS TWO D.C. LEVELS - 70 V AND 150 V. THE D.C. LEVEL CHANGES EVERY 0.5 SEC.

NOTE ii: REMOTE RESET OF BERKELEY SCALER.

Figure 11. Automatic Reset for Time Interval Counter.

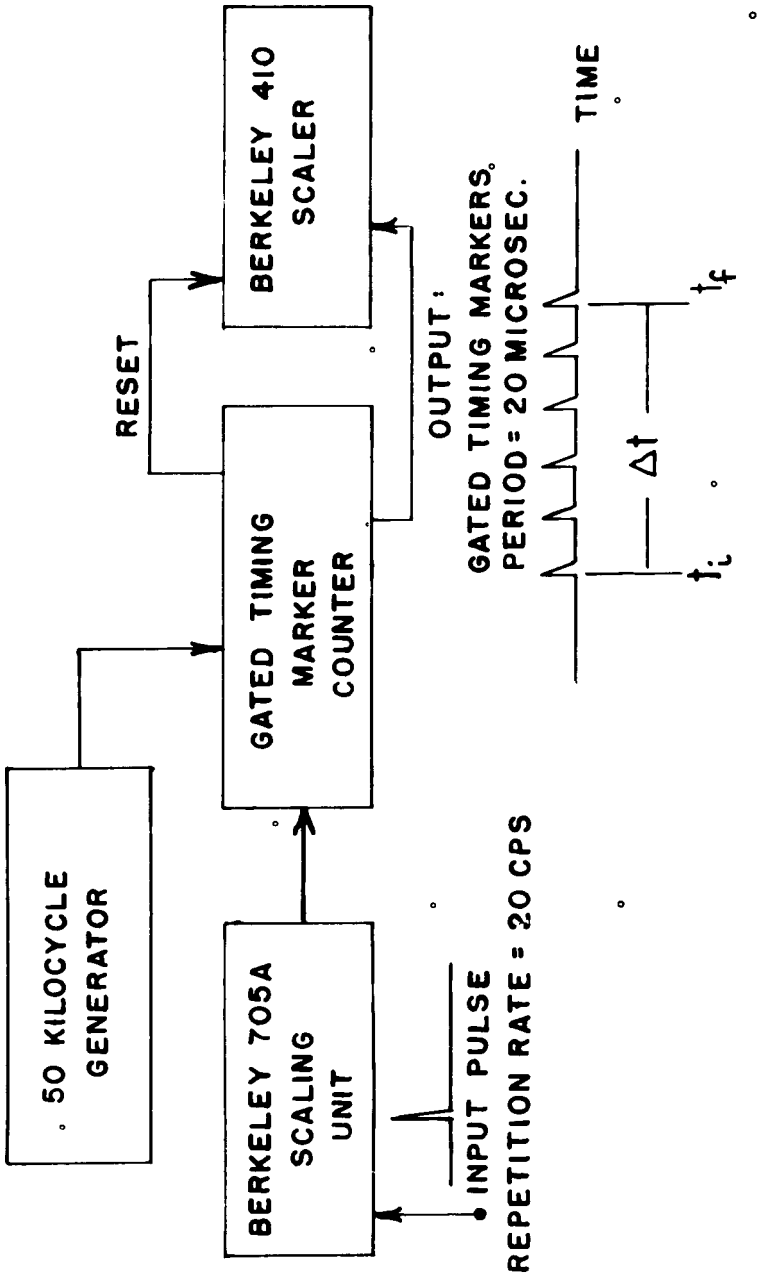


Figure 12. Systems Schematic for Time Interval Counter.

analyzer.

Two well regulated sources of D.C. power are used; one source is used to provide a current of approximately 10 amperes through a length of voice-coil wire while the other source energizes the magnetic field of the analyzer. Voice-coil wire is necessary because it is pliable, has small mass per unit length, and will not overheat with 12 amperes of current through it. A balance pan is tied to one end of the wire and hangs over a wheel rim. Balance weights in the pan are used to put various values of tension on the wire. The pivot at the other end of the wire is placed at the target wire position. The target pin wheel is removed from the electron scattering chamber during this magnet calibration.

If that portion of the wire, midway between the pivot and the balance wheel, passes through the magnetic field of the analyzer, the wire in the field will have a radius of curvature r (meters), which is determined by I (amperes), the current in the voice-coil wire, B (webers/meter^2), the magnetic field between pole faces, and T (Newtons), the tension necessary to hold the wire in the magnetic field. The following relationship exists among these quantities:

$$T = IBr \ . \qquad (2.2.1)$$

Since B is a function of current, I_m, in the magnet coils, one can experimentally determine the tension necessary to suspend the wire on a fixed trajectory between the pole faces of the magnet for various values of the magnetic field. The results of these measurements are shown in Figure 13.

The momentum of an electron having the same trajectory through the magnet air gap as the wire can be related to the magnet current as

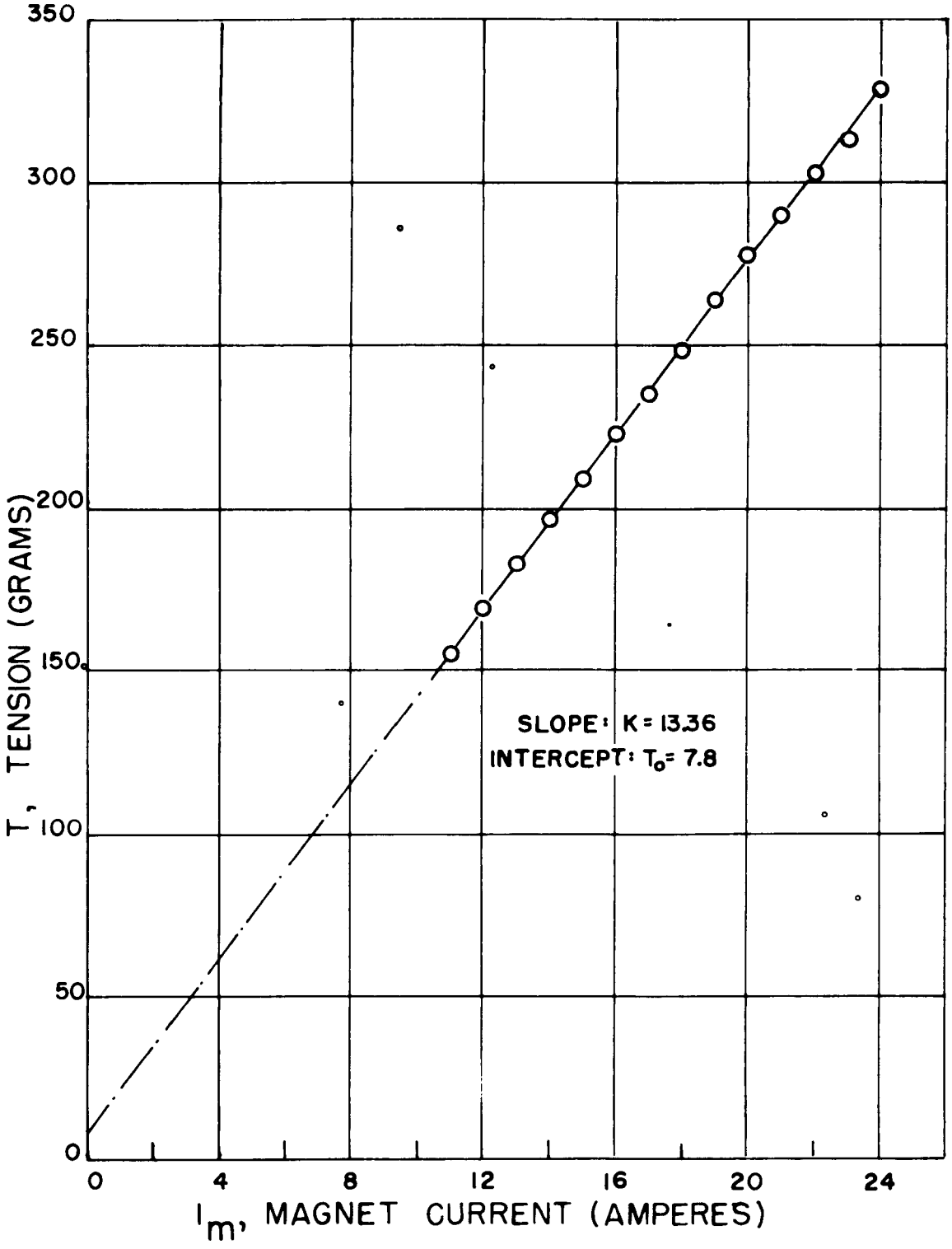


Figure 13. Calibration Curve for Analyzer Magnet.

follows:

$$eBr = p \qquad (2.2.2)$$

thus,

$$T/I = p/e = mc\eta/e$$

$$= 1704.3 \times 10^{-4}\eta \text{ webers/meter} . \qquad (2.2.3)$$

η is momentum in units of mc, where m is the rest mass of the electron.

A least square fit for the points on the graph of Figure 13 shows,

$$T - T_o = KI_m . \qquad (2.2.4)$$

Putting equation (2.2.4) into (2.2.3) gives

$$(KI_m + T_o)/I = 1704.3 \times 10^{-4}\eta . \qquad (2.2.5)$$

The calibration determines all quantities on the left side of equation (2.2.5).

Slit Alignment

After the hot wire experiment is completed, the wire is put into an equilibrium position and the front and back collimating slits are positioned so that the wire goes through the center of both slits. The slit housing brackets are used to align the front slits, and the bracket holding the back slit and the detector counter barrel is used to align the back slits.

A cathetometer is placed in the median plane of the synchrotron 12 inches below the detector counter (see Figure 4). The cross hairs on the cathetometer are focused on the center of the front slit aperture in order to check the centering of the hot wire with the slit aperture. The wire is removed, and the cross hairs are focused on the target wire. The magnet can be pivoted about the axis AA' (see Figure 4) in order to align the slit aperture with the target wire and the cathetometer cross

hairs. The cathetometer is now used to check the alignment of the front slit with the target for all seven scattering angles; this is accomplished by moving the pivot about which the analyzer magnet and its cart moves. This pivot point lies 13½ inches above the target wire and can be moved in two perpendicular directions by means of set screws. Adjustment of the pivot point is completed when the target wire, front slit aperture, and cathetometer cross hairs are colinear to 1/32 of an inch for all seven scattering angles.

Measurement of Scattering Angles

The average incident momentum direction is measured by using photographic methods to determine the direction of the Bremsstrahlung cone that is formed when the beam collides with the target wire (26). Heitler (27) has shown that the ratio of base to height of this Bremsstrahlung cone is of the order mc^2/E_o, where E_o is the incident electron energy. For this experiment this ratio is about 1/120 so that the Bremsstrahlung cone is well defined and can be used to determine the direction of incident momentum of the electrons. A transit is fastened to the top of the scattering chamber so that its plumb line is aligned with the target wire. This alignment is achieved by using a cathetometer placed in several widely separated positions. The transit is then used to measure the azimuthal angle between the vertical plane containing the axis of the front collimating slit of the detector system and the vertical plane containing the following two points: (1) the point at which the beam strikes the target wire, and (2) a point lying 20 feet from the target wire, through which the Bremsstrahlung beam is known to pass. This latter point was determined photographically by Cline (26). This azimuthal angle is referred to as the scattering angle through which

the electrons are deflected before being detected by the detector counting system.

The measurement of the scattering angle was made several times; one-fourth of a degree is the estimated error of these measurements. A protractor is placed above the scattering chamber, and a pointer fastened to the analyzer magnet yoke facilitates the measurement of the scattering angle during experiments on electron scattering.

Determination of Analyzer and Counter Response

With the slit alignment complete and lead shielding packed between the synchrotron and the detector counter, several preliminary scattering experiments are done in order to determine background and to determine the integral discrimination setting to be used on the linear amplifier and discrimination circuit.

The analyzer current is turned on and varied until counts are recorded in the scalers. An oscilloscope is used to check the appearance of pulses that are being counted. An integral discrimination curve is run; Figure 14 shows the plot of counting rate (detector counts per monitor count) versus the discrimination level. The level is set at the midpoint of the integral discrimination plateau, and a momentum spectrum (see Figure 5) is obtained with a fixed discrimination level.

The front slit collimator is blocked by putting a solid cylinder into the slit housing. In runs lasting for several hours longer than the normal run used in obtaining final experimental data, no counts were observed; this indicates that every detected count is due to electrons that pass through the front collimating slit. The counting rates with an unblocked slit for short periods of time are recorded in the histogram shown in Figure 15. The average in this typical case is 18

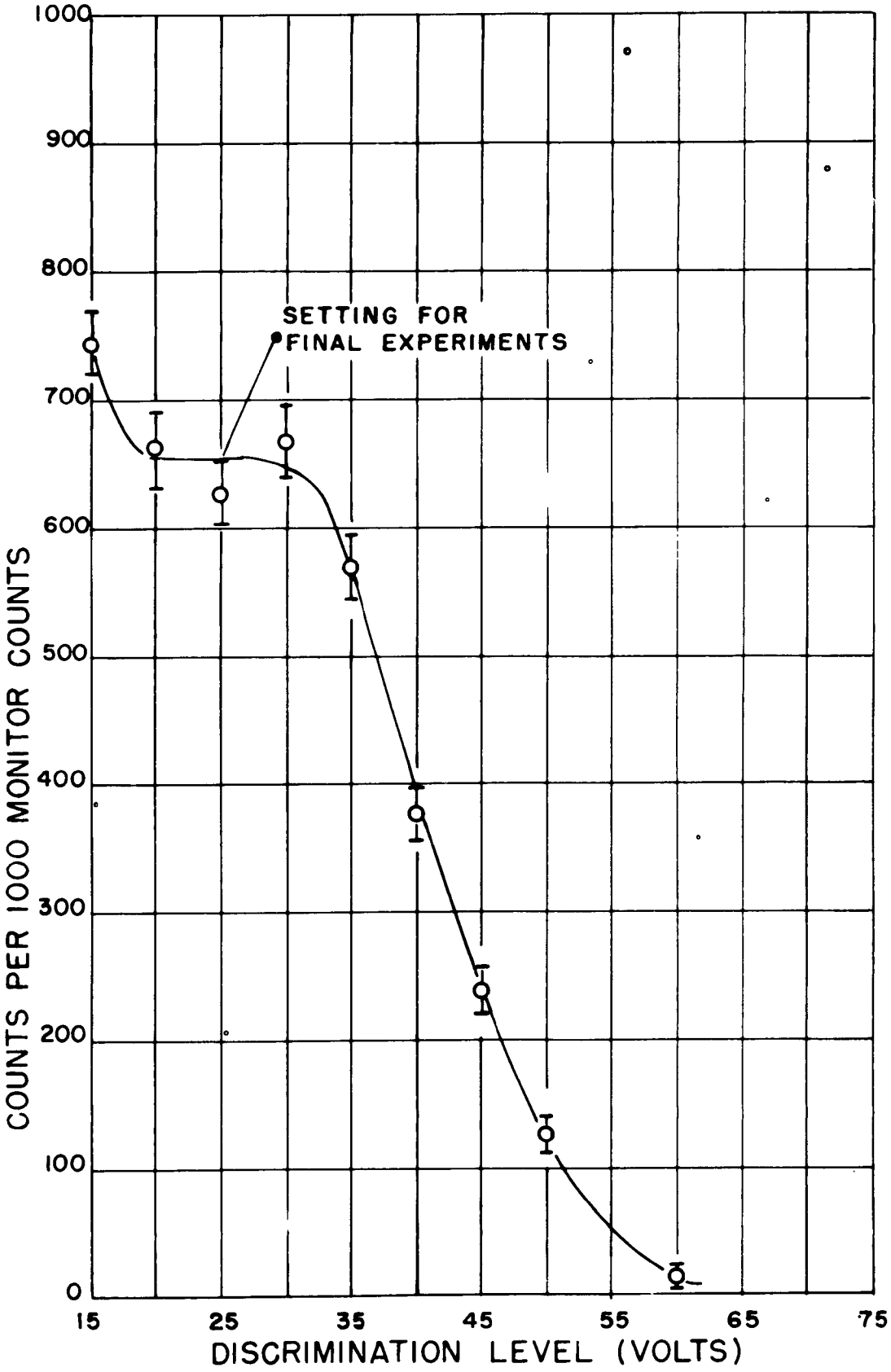


Figure 14. Integral Pulse Height Discrimination Curve.

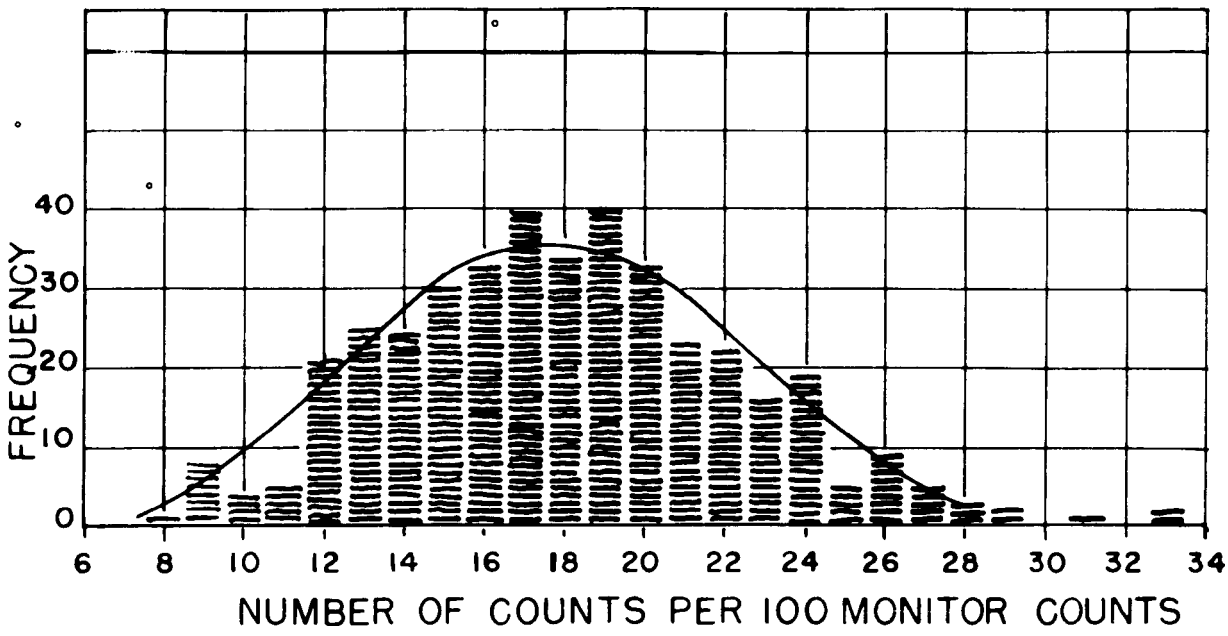


Figure 15. Histogram of Random Counting.

counts/monitor with an expected deviation of 4 counts/monitor count. The system is thus shown to be counting randomly.

Selection of Beam Energy

Reference to the momentum spectrum (Figure 5) shows that the elastic peak occurs at an analyzer current I_m of 18 amperes. Substituting this value of the analyzer current into the equation (2.2.5) makes $\eta = 121.49$ units of mc. Errors in this measurement are due to friction in the balance wheel, to neglecting the weight of the wire, and to the measurement of the current in the "hot" wire. These are estimated to contribute an error of order 2 percent.

Measurements made by Randolph (25) show that the peak guide field, B_o, at equilibrium orbit of the accelerated electrons is 2884.5 gauss; the radius of the orbit, r, is 102.7 ± 1.0 cm; and the frequency, f, of the guide field alternations is 20.1 cps.

$$\eta = \frac{eBr}{mc} = \frac{B_o r \sin\omega t}{1704.3} ,$$

where

$$B_o r = 296{,}238 \text{ gauss-cm}$$

$$\omega t = 40.2\pi t \text{ radians} .$$

Errors involved in this experiment are principally due to measuring the field strength in a small region of space through which the beam's equilibrium orbit goes, with apparatus which can only determine average field strength over a relatively large volume. The radius of the equilibrium orbit is determined by the formula,

$$2\pi r + 4L = c/\nu ,$$

where L is the effective length of one of the synchrotron's straight sections; ν is the frequency of revolution of the accelerating electrons; and c is the velocity of light. The frequency of the guide field alter-

nations is measured by using a harmonic analyzer. The time interval counter monitors the beam acceleration time during experiments. The acceleration times in this experiment are set at 5774 microseconds with fluctuations of 100 microseconds due to the instability of the synchrotron during long operating periods. This fluctuation causes a 2 percent error in the measurement of the beam energy.

The measurement of the beam energy by the two experiments mentioned above is listed in Table 1. An estimate of their deviation is also included.

TABLE 1

MEASUREMENTS OF BEAM ENERGY

"Hot" Wire Measurement	Field Measurement
η = 121.49 ± 3.30	η = 115.80 ± 3.20
E = 62.07 ± 1.68 mev	E = 59.16 ± 1.64 mev

The average of these two measurements (60.61 mev) is the value chosen for this experiment.

Raw Data

Table 2 records the numbers resulting from these electron scattering experiments. Each number was recorded directly from the detector scalers and the monitor scalers. Each run (count for fixed angle and fixed target) was repeated five times in order to establish a measured mean and deviation.

Table 3 is the same as Table 2 except that a different photomultiplier tube was used in the detector counter because the original tube became defective during the final series of experiments. Table 4

and Figure 16 give some typical examples of momentum spectra taken at different scattering angles.

TABLE 2

UNPROCESSED EXPERIMENTAL DATA (GROUP I)

Run	52°	65.5°	76.75°	89.25°	103.25°	116.25°
Aluminum						
1	3898	2383	2815	2972	2894	1822
2	3779	2070	3210	2864	2951	1957*
3	3637	2024	3444	2983	2831	
4	3529	1770	3111	2724	2965	
5	3690	1796	2947	2761	2851	
6		1764				
N_m	500	1000	4000	10000	20000	30000
Copper						
1	7926	4751	7405	7444	5635	3091
2	8039	4468	7379	6755	5719	3145
3	7460	4785	7249	7111	5677	3010*
4	7945	4527	7469	7235	5669	
5	7232	4634	7292	7093	5617	
N_m	500	1000	4000	10000	20000	30000
Tungsten						
1	9922	4097	4988	4002	2548	1341
2	8880	3962	5113	3989	2485	1381
3	9224	3809	5276	4026	2508	1409*
4	8539	4272	5281	4032	2411	
5	8139	4185	5005	3811	2438	
N_m	500	1000	4000	10000	20000	30000

N_m is the number of monitor counts.

*Photomultiplier became defective at this point.

TABLE 3

UNPROCESSED EXPERIMENTAL DATA (GROUP II)

Run	65.5°	116.25°	128°
Aluminum			
1	2149	2152	1025
2	2213	2183	1025
3	2084	2292	1049
4	2262	2196	1021
5	2202	1987	1018
6		2164	
N_m	1000	30000	30000
Copper			
1	4497	3497	1559
2	4614	3526	1674
3	4619	3520	1652
4	4858	3553	1654
5	4581	3533	1635
6		3228	
N_m	1000	30000	30000
Tungsten			
1	4061	1700	730
2	4065	1674	702
3	3873	1609	685
4	4010	1542	719
5	4152	1532	729
6	4131	1621	
7	4042		
N_m	1000	30000	30000

N_m is the number of monitor counts.

TABLE 4

MOMENTUM SPECTRA FOR ALUMINUM TAKEN AT THREE SCATTERING ANGLES

I_m	65.5°	89.25°	116.25°
0	0	3	0
4	0	0	0
6	0	0	
8	0	2	1
10	4	11	
12	11	29	4
14	21	40	
16	176	218	74
17	711	812	337
18	1968*	2861*	720*
19	740	638	303
20	112	86	34
24	13	7	9
N_m	1000	5000	10000

*Mean values of several readings.

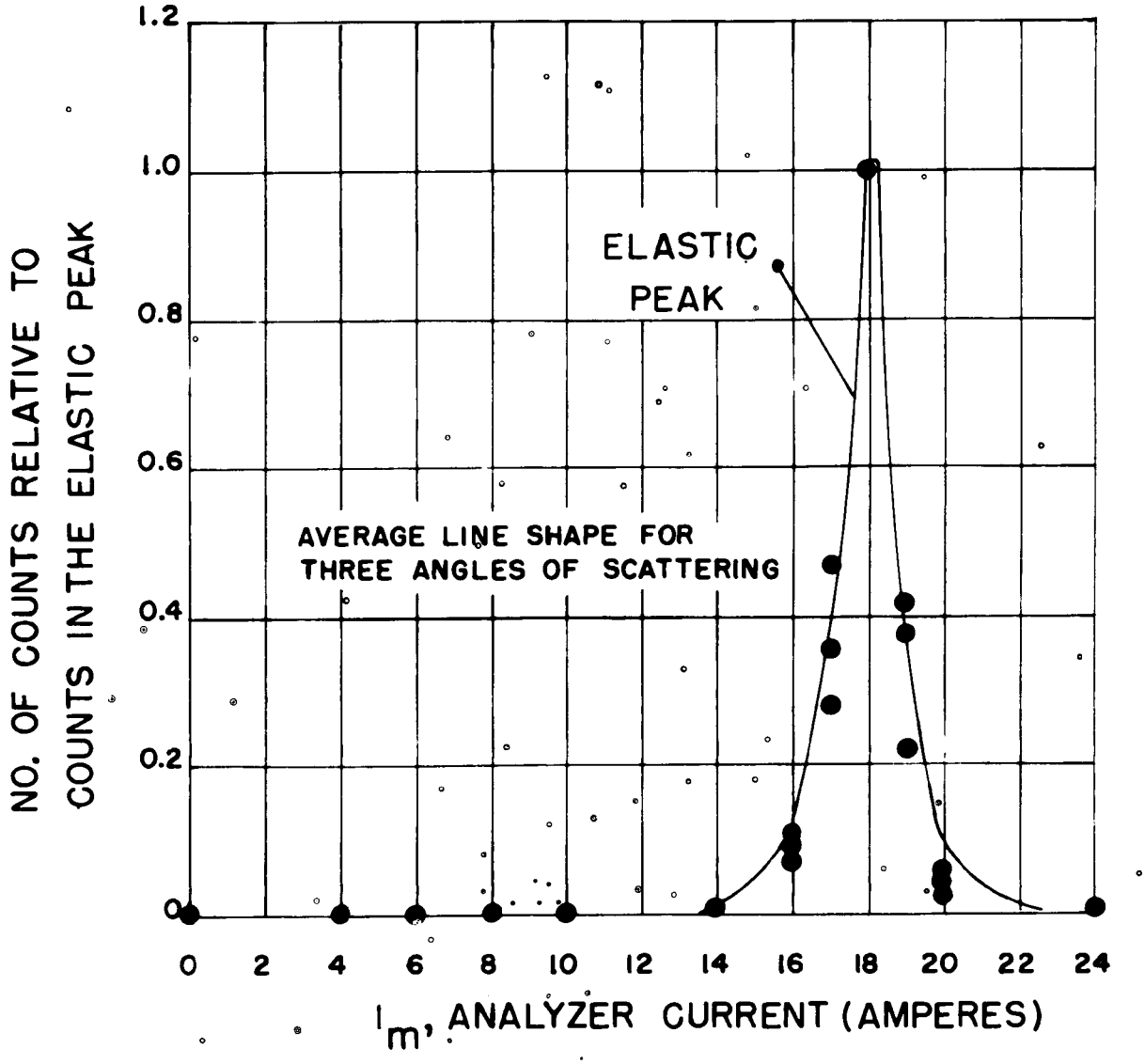


Figure 16. Normalized Momentum Spectra for Scattering Angles of 52°, 76.25°, 90°, and 103°.

CHAPTER III

CORRECTIONS TO EXPERIMENTAL DATA

The process of single elastic scattering of high energy electrons from nuclei in target foils of finite thickness is always accompanied by other processes such as multiple scattering, plural scattering, and Bremsstrahlung radiation. These accompanying processes tend to obscure the true elastic scattering counting rates observed by any detection system of finite aperture and finite energy resolution. It is the purpose of this chapter to show that effects such as these give rise to negligible corrections to the data of this experiment.

Counting Losses

C.H. Westcott (28) has determined an approximate formula for counting losses incurred when counting particles from pulsed sources. The formula is given in the following equation:

$$E' = \mu T(1 - \mu\tau') \qquad (3.1.1)$$

where

E' = expected count,

μT = true count,

μ = true counting rate,

T = total counting time,

$\tau' = (1 - \frac{\tau}{2T})\frac{\tau}{f}$, effective dead time,

where

τ = measured dead time of detecting apparatus,

T = pulse length (time during which particles are entering detection equipment), and

$pT = f$ = duty cycle or the fraction of the total counting time, T, that the particles are entering the detection system. The quantity, p , is the repetition rate of the pulse of particles.

It is assumed that the counting rate within the pulse interval, T , is a constant and that $\tau << T$. Measurements indicate that in this experiment

$$\tau = 1 \times 10^{-6} \text{ seconds}$$

$$T = 30 \times 10^{-6} \text{ seconds}$$

$$f = pT = 20 \times 30 \times 10^{-6} = 6 \times 10^{-4} \text{ seconds.}$$

Therefore, the effective dead time for these experimental conditions is

$$\tau' = (1 - \frac{1}{60}) \frac{10^{-6}}{6 \times 10^{-4}} = 0.164 \times 10^{-2} \text{ sec.}$$

The statistical estimates of the true counting rates are never greater than 4 counts/second so that from equation (3.1.1) one has

$$E' = \mu T (1 - 4 \times 0.164 \times 10^{-2}) \quad , \text{ or}$$

$$(E' - \mu T) \div \mu T = -0.007.$$

Counting losses, therefore, are less than 0.7 percent and are neglected in this experiment.

The Radiation Loss

The probability that an electron has an energy greater than $E_o - k$ after penetrating a target of thickness $\bar{l}$ is given by Heitler (27) as:

$$w(y)dy = \frac{e^{-y} y^{b\bar{l}-1}}{\Gamma(b\bar{l})} dy \quad , \tag{3.2.1}$$

where

$$y = \log \frac{E_o}{E_o - k} \quad ,$$

E_o = incident beam energy,

k = energy lost to radiation, and

b = constant characteristic of scattering target.

$\Gamma(b\bar{1})$ is the Gamma function.

The correction to the observed number of scattered electrons n_o is given by the formula:

$$n_t = n_o + \int_o^\infty R(y)\, w(y)\, dy . \qquad (3.2.2)$$

R(y) is the energy resolution of the detection system, and n_t is the total number of electrons scattered.

The probability that a collision will take place in a thickness, dx, after penetration of the target to a distance, x, is

$$P(x)dx = e^{-\alpha x} dx ,$$

where α is the absorption coefficient characteristic of the scattering material. If $\alpha d << 1$, where d is the target thickness, then this probability distribution is approximately constant. From this it can easily be shown that the average path length, $\bar{d}$, before at least one collision occurs, is:

$$\bar{d} = d/2 ;$$

that is, on the average the collisions take place in the center of the target wire, and the average path length, therefore, is independent of the scattering angle at which the detection system is placed. From equations (3.2.1) and (3.2.2) one can see that the quantity, $n_t \div n_o$ is independent of the scattering angle. Because this experiment is a measure of scattering cross section relative to the scattering angle of 52^o, no correction due to radiation loss is required for the observed data. This conclusion is true for any thin target which has cylindrical symmetry and whose symmetry axis coincides with the axis of rotation

of the detection system.

Multiple Scattering

The theory of multiple scattering has been treated by Molière (29), by Goudsmit and Saunderson (30), and by Bethe (31). Experiments of Hanson et al, using thin foils, agree with the theoretical results of Bethe who has also summarized the work of Molière, and of Goudsmit and Saunderson.

Chase and Cox (32) indicate that observing single scattering from target foils with a detection system having a finite aperture requires the following correction to multiple scattering:

$$I_o = I_s\left\{1 + \frac{\epsilon^2}{4}\left(\frac{\sigma'(\theta)}{\sigma(\theta)}\cot\theta + \frac{\sigma''(\theta)}{\sigma(\theta)}\right)\right\} \qquad (3.3.1)$$

$$= I_s\{1 + \delta(\theta)\}.$$

I_o is the observed counting rate, and I_s is the single scattering rate; δ is the percent correction. The primes indicate differentiation with respect to angle.

Hanson et al (33) indicate that:

$$\epsilon^2 = \chi_c^2 (B - 0.7),$$

where

$$\frac{\chi_c^2}{\chi_a^2} = \frac{7e^B}{6B}$$

$$\chi_c^2 = \{4\pi N\bar{t} Z(Z+1)e^4\} \div (pv)^2$$

$$\chi_a^2 = \left\{\frac{\hbar Z^{1/3}}{0.885 a_o}\right\}^2 \left\{1.13 + 3.76\left(\frac{Z}{137\beta}\right)^2\right\},$$

in which

N = number of scattering atoms per cm^3,

$\bar{t}$ = average thickness of scattering foil,

V = speed of incident electrons,

a_o = Bohr radius, and,

Z = atomic number.

The necessary quantities for calculating the correction, δ, have been tabulated in Table 5. The first and second derivatives of the scattering cross section have been estimated by first and second differences. Results in this table indicate that the correction due to the superposition of multiple scattering on single scattering is negligible.

TABLE 5

MULTIPLE SCATTERING CALCULATIONS

θ	$\frac{\epsilon^2}{4}$	$\frac{\sigma'}{\sigma}\cot\theta+\frac{\sigma''}{\sigma}$	$\delta(\theta)$	$1+\delta(\theta)$	$\frac{1+\delta(\theta)}{1+\delta(\theta_o)}$
Tungsten	4.1 (-4)*				
52°		-12.02	-49.28 (-4)	.995	1.
66°		- 9.27	-38.00 (-4)	.996	1.001
77°		- 7.38	-30.48 (-4)	.997	1.002
89°		- 5.95	-23.39 (-4)	.998	1.003
103°		- 3.60	-13.76 (-4)	.999	1.004
116°		- 1.70	- 6.97 (-4)	.999	1.004
129°		- 0.52	- 2.13 (-4)	.9997	1.005
Copper	3.77 (-4)				
52°		-.9.94	-37.47 (-4)	.996	1.
66°		- 7.01	-26.42 (-4)	.997	1.001
77°		- 5.57	-20.99 (-4)	.998	1.002
89°		- 4.39	-16.55 (-4)	.998	1.002
103°		- 3.22	-12.13 (-4)	.999	1.003
116°		- 2.12	- 7.99 (-4)	.999	1.003
129°		- 0.81	- 3.05 (-4)	.9996	1.004
Aluminum	4.70 (-4)				
52°		- 8.69	-40.84 (-5)	.9995	1.
66°		- 6.70	-31.49 (-5)	.9996	1.0000
77°		- 5.24	-24.62 (-5)	.9999	1.0004
89°		- 4.07	-19.12 (-5)	.9999	1.0004
103°		- 2.95	-13.86 (-5)	.9999	1.0004
116°		- 1.95	- 9.16 (-5)	.9999	1.0004
129°		- 0.74	- 3.47 (-5)	.9999	1.0004

*(-4) means x 10^{-4}.

**Last column is the correction relative to the angle $\theta_o = 52°$.

Double Scattering

There is a finite probability that an electron will be scattered 90° in a direction parallel to the axis of the target wire and then scatter again through an angle of 90° into the detection system. This is a double scattering event tending to increase the observed counts at each scattering angle and may necessitate a correction to the data. Figure 17 graphically portrays such a double scattering event in which an electron at point S is scattered through an angle θ' into the solid angle, $d\Omega' = \sin\theta' d\theta' d\phi'$, where ϕ' is the azimuthal angle about the direction OS. After traversing the target material a distance SD = R, it is again scattered by an amount θ'' into the solid angle, $d\Omega'' = \sin\theta'' d\theta'' d\phi''$ where ϕ'' is the azimuthal angle about the direction SD. Angle, $d\Omega''$, is the solid angle defined by the aperture of the detection system.

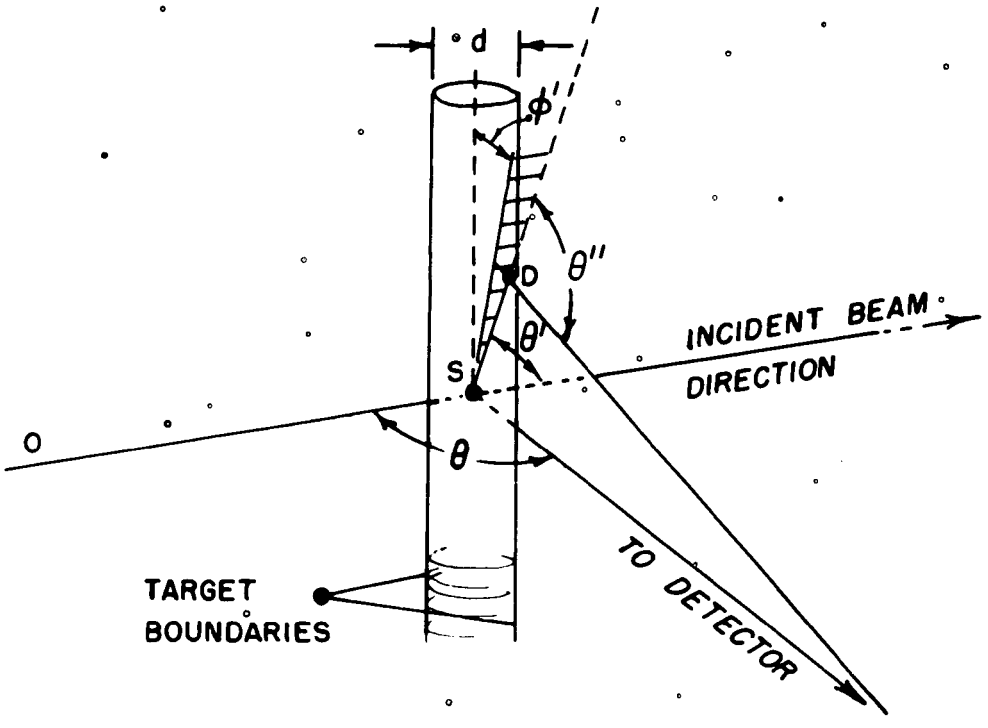


Figure 17. Double Scattering In The Target Wire.

The largest contribution to the counting rate, at any given scattering angle at which the detection system is placed, comes from the single scattering event in which an electron scatters through an angle, θ, into the solid angle, $d\Omega = \sin\theta\, d\theta\, d\phi$ where ϕ is the azimuthal angle about the direction OS. The solid angle, $d\Omega$, is approximately equal to $d\Omega''$ and can be defined by the aperture of the detection system.

The correction to double scattering is found by considering the contribution of both the single scattering and the double scattering events to the probability that an electron will enter the detecting system. This probability is given by the formula,

$$Nt\sigma(\theta)\, d\Omega = Nt\sigma_s(\theta)\, d\Omega + \iint_{\Omega'} Nt\sigma_s(\theta')\, \sigma_d(\theta'')\, N R(\theta',\phi')\, d\Omega'\, d\Omega'' \qquad (3.4.1)$$

where

N is the number of scattering atoms per cubic centimeter;

t is the target thickness in cm; and,

R is the distance, in cm, traversed in the target between the first and second scattering, and is a function of θ' and ϕ'.

Now, the total number of counts observed through $d\Omega$ is given by the formula,

$$I(\theta) = Nt\sigma(\theta)\, d\Omega ,$$

and if one assumes that

$$d\Omega \simeq d\Omega''$$

$$\sigma_d(\theta'') \simeq \sigma_d\left(\theta'' = \frac{\pi}{2}\right),$$

then, the equation (3.4.1) becomes

$$I(\theta) = I_s(\theta)\left\{1 + \frac{N\sigma_d(\theta''=\frac{\pi}{2})}{\sigma(\theta)} \int_0^{\pi} \int_{\chi_c}^{\pi} R(\theta',\phi')\, \sigma_s(\theta')\, d\Omega' \right\} \qquad (3.4.2)$$

where $I_s(\theta)$ is the total number of counts due to single scattering only, and $I(\theta)$ is the total number of counts due to single and double scattering. The lower limit on the integral for θ' is a characteristic angle in the theory of multiple scattering; physically it means that an average of one single scattering occurs for angles greater than χ_c. For target thicknesses used in this experiment, $\chi_c = 5$ degrees.

The correction due to double scattering is the second term within the parentheses of equation (3.4.1). Its magnitude can be estimated by determining the upper bounds of the integrand, $R(\theta',\phi')\,\sigma(\theta')$.

For $\theta' = 5^\circ$,

$\sigma(\theta' = 5^\circ) \simeq 10^{-25}\ cm^2$ (from homogeneous model calculations)

$R(\theta' = 5^\circ, \phi') = 0.005$ cm ($\frac{1}{2}$ target thickness)

and for $\theta' = 90^\circ$,

$\sigma(\theta' = 90^\circ) \simeq 10^{-27}\ cm^2$

$R(\theta' = 90^\circ, \phi') = 0.1$ cm.

By considering that the electron may be multiply scattered out of the target before a second large angle scattering can occur, or that the electron may not be detected because of energy loss due to Bremsstrahlung radiation, Hammer (19) obtained an estimate of 0.9 cm for the quantity, $R(\theta',\phi')$. Since the scattering cross section is a monotonic decreasing function of the scattering angle, θ', and since the upper bound of the distance, $R(\theta'\phi')$, traversed between the first and second scatterings is about 1 cm, one concludes that:

$$\sigma(\theta')\,R(\theta',\phi') \leq 5\times 10^{-28}\ cm^3 \qquad \text{for all scattering angles.}$$

Thus,

$$\int_0^{\pi}\int_{\chi_c}^{\pi} R(\theta'\phi')\,\sigma(\theta')\,d\Omega' \leq 5\times 10^{-28}(2\pi) \simeq 3\times 10^{-27}$$

For the three targets used in this experiment,

$N \simeq 5 \times 10^{22}$ atoms/cm^3 ,

$$\frac{\sigma(\theta'')}{\sigma(\theta)} \leq 10 \text{ where } \theta > \theta'' = 90^\circ,$$

$$\frac{\sigma(\theta'')}{\sigma(\theta)} \leq 1 \text{ for } \theta < \theta'' = 90^\circ.$$

The magnitude of the correction term is then,

$$\frac{N\sigma(\theta=90^\circ)}{\sigma(\theta)} \int_0^{\pi} \int_{\chi_c}^{\pi} R(\theta\phi)\,\sigma(\theta)\,d\Omega \leq 5\times10^{22}\times10\times3\times10^{-27} = 1.5\times10^{-3}.$$

This is a correction of less than 0.2 percent at a scattering angle of about 128° and is neglected in this experiment. At scattering angles less than 128° the correction is much less than 0.2 percent.

Geometric Corrections

Because the detection system has a finite circular aperture, a correction for finite solid angle is required. In this section it is shown to be negligible.

In Figure 18 the Z-axis represents the center line of the detection system. The angle, θ, is the scattering angle of a detected electron which has been deflected along the Z-axis; whereas, θ' is the scattering angle of a detected electron which has not been deflected along the Z-axis. The angle, $0 \leq \epsilon \leq \alpha$, is a small angle relative to θ and θ' between the Z-axis and the direction OP; $0 \leq \phi \leq 2\pi$ is the azimuthal angle; α is the angle which essentially defines the aperture of the detection system. The solid angle, Ω' , is defined by this aperture.

From spherical trigonometry it can be shown that the following relationship exists among the angles indicated in Figure 18:

$$\cos\theta' = \cos\theta\cos\epsilon + \sin\theta\sin\epsilon\cos\phi,$$

or since, $\sin\epsilon \simeq \epsilon$

$$\cos\theta' \cong \cos\theta\left(1-\frac{\epsilon^2}{2}\right) + \epsilon\sin\theta'\cos\phi. \qquad (3.5.1)$$

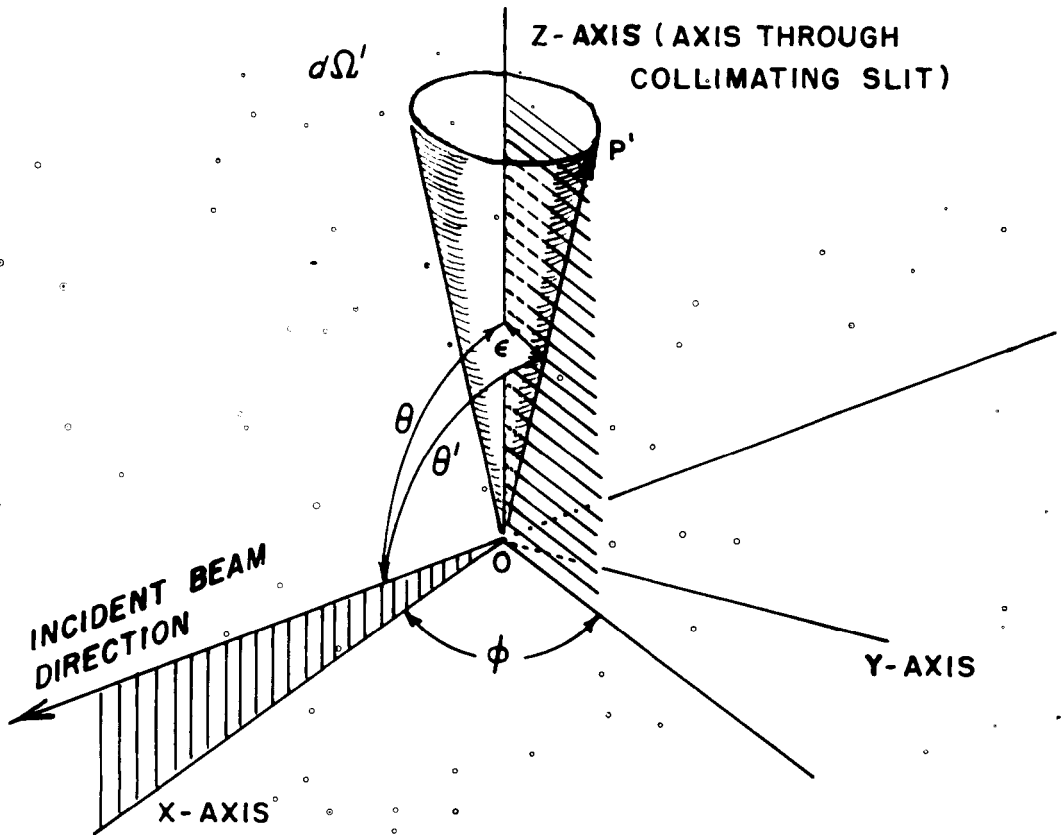


Figure 18. Geometric Correction to Single Scattering

Defining $h \equiv \Theta' - \Theta$, where h is small, the Taylor expansion for $\cos\Theta'$ is

$$\cos\Theta' = \cos\Theta - \sin\Theta h \qquad \text{(to first order)} \qquad (3.5.2)$$

$$\cos\Theta' = \cos\Theta - \sin\Theta h - \cos\Theta\frac{h^2}{2} \qquad \text{(to second order)} \qquad (3.5.3)$$

Substituting equation (3.5.1) into equation (3.5.2) and solving for h, one can substitute this result in place of h^2 into equation (3.5.3). Neglecting all terms of order ϵ^3, one has the following result:

$$h = \theta' - \theta = -\epsilon\cos\phi + \frac{1}{2}\epsilon^2\cot\theta\sin^2\phi \qquad (3.5.4)$$

A Taylor series expansion of the scattering cross section to sec-

ond order is

$$\sigma(\theta') = \sigma(\theta) + \sigma'(\theta)h + \frac{1}{2}\sigma''(\theta)h^2 . \qquad (3.5.5)$$

The observed intensity is, then, proportional to the average of $\sigma(\theta')$ over the solid angle Ω' . Thus,

$$I_0 \simeq \int_{\Omega'} \sigma(\theta')\, d\Omega' \div \int_{\Omega'} d\Omega' = \frac{1}{\pi a^2}\left\{\sigma(\theta)\int_{\Omega'} d\Omega' + \sigma'(\theta)\int_{\Omega'}(\theta'-\theta)\, d\Omega' + \frac{\sigma''(\theta)}{2}\int_{\Omega'}(\theta'-\theta)^2\, d\Omega'\right\}$$

where $d\Omega' \simeq \epsilon\, d\epsilon\, d\phi$.

Since the theoretical intensity along the Z-axis is also proportional to $\sigma(\theta)$, one can write:

$$\frac{I_0}{I_t} = \left\{1 + \frac{1}{\pi a^2}\left(\frac{\sigma'(\theta)}{\sigma(\theta)}\int_{\Omega'}(\theta'-\theta)\, d\Omega' + \frac{\sigma''(\theta)}{\sigma(\theta)}\int_{\Omega'}(\theta'-\theta)^2\, d\Omega'\right)\right\}$$

$$= 1 + \frac{a^2}{8}\left\{\frac{\sigma''(\theta)}{\sigma(\theta)} + \cot\theta\,\frac{\sigma'(\theta)}{\sigma(\theta)}\right\} . \qquad (3.5.6)$$

In this experiment, $a \simeq 0.250'' \div 13'' = 1 \div 52$. Reference to Table 5 shows that the upper bound of the term in braces of equation (3.5.6) is 50. One gets

$$\frac{I_0}{I_t} \leq 1 + \frac{50}{8(52)^2} \simeq 1.0023 .$$

This is a correction of approximately 0.2 percent and will be neglected in this experiment.

Energy Loss from Nuclear Recoil

Hofstadter (13) has shown that the recoil kinetic energy of a nucleus struck by an electron is given by the following equation:

$$\Delta E = \frac{E_0^2}{Mc^2}\left\{1 - \cos\theta\right\} \div \left\{1 + \frac{E_0}{Mc^2}(1 - \cos\theta)\right\}$$

where

E_0 = incident electron energy

Mc^2 = rest energy of struck nucleus.

Considering the lightest nucleus in this experiment, we have:

$$Mc^2 \simeq 27 \times 938$$

$$\frac{E_o^2}{Mc^2} \simeq \frac{60.6^2}{27 \times 938} = 0.103$$

$$\frac{E_o}{Mc^2} \simeq 0.00236$$

so that

$$\Delta E \cong 0.103 \frac{1 - \cos\theta}{1 + .00236(1 - \cos\theta)} \cong 0.103(1 - \cos\theta)$$

$$\leq 0.103 \text{ mev}.$$

This is well within the limits of the energy resolution of the detection system used in this experiment.

CHAPTER 4

DATA PROCESSING OF EXPERIMENTAL RESULTS

Introduction

The average detector count and the estimated standard deviations corresponding to these averages are taken from Tables 2 and 3 and put into a form suitable for comparison with theoretical cross sections. Since the incident beam flux is not a directly measured quantity in this experiment, the experimental data cannot be used to determine absolute scattering cross sections. Only a comparison relative to a fixed angle is possible. The experimental data, therefore, are compared here relative, for example, to the scattering angle of 52 degrees; that is, the data are "normalized" arbitrarily to the scattering angle of 52 degrees. Consequently, this procedure determines only the shape of the scattering cross section as a function of scattering angle.

The computations for scattering cross sections are for a potential energy function corresponding to a homogeneous distribution of nuclear charge and to a shell distribution of nuclear charge. These are usually referred to as homogeneous model and shell model nuclear distributions, respectively.

The computations to which the experimental results are compared are made by using an IBM 650 digital computer. The method of computation follows that of Yennie, Ravenhall, and Wilson (34). Preliminary computations for the homogeneous and shell model were checked against those of A.E. Glassgold (35).

The values of r_o, a constant of proportionality in the $A^{1/3}$ Law, for aluminum, copper, and tungsten are compared to those of Hofstadter (12) and Pidd and Hammer (24).

Discussion of Results from IBM 650 Digital Computer Calculations

The calculation to which the data of this work are fitted is based on a power series solution of the Dirac equation under the assumption that $W >> mc^2$ where W is the kinetic energy of the scattering electron. A potential energy function, due either to a homogeneous or shell distribution of nuclear charge, is assumed. This power series solution is an expansion about the point $kr = 0$. A numerical integration (fourth order Runge-Kutta integration technique) with a power series solution for $kr = 0.1$ as the initial value determines the solutions of Dirac's equation to a value of $kR = x_o$ called the "fitting on" radius. These solutions are set equal to a linear combination of Coulomb wave functions

$$F_j(x_o) = C_j F_j^{+}(x_o) + D_j F_j^{-}(x_o)$$

$$G_j(x_o) = C_j G_j^{+}(x_o) + D_j G_j^{-}(x_o) \quad , \qquad (4.1.1)$$

where $F_j(x_o)$ and $G_j(x_o)$ are the numerical solutions to the Dirac equation; $F_j^{+}(x_o)$ and $G_j^{+}(x_o)$ are regular Coulomb functions, and $F_j^{-}(x_o)$ and $G_j^{-}(x_o)$ are the irregular Coulomb functions. The quantity, j, is the total angular momentum quantum number. These equations determine the ratio C_j/D_j. The phase shift due to the effect of a non-Coulomb potential is determined by the equation:

$$\tan(\eta_j - \eta_j^c) = \frac{\sin(\eta_j'^c - \eta_j^c)}{C_j/D_j + \cos(\eta_j'^c - \eta_j^c)} \quad . \qquad (4.2.2)$$

where η_j is the jth phase shift due to the finite size of nuclear charge distribution; η_j', the jth irregular Coulomb phase shift; and η_j^c, the jth regular Coulomb phase shift. The difference between the Coulomb phase shifts is determined from:

$$\exp i(\eta_j'^c - \eta_j^c) = \frac{1 - i\tan\pi(j+1/2-\rho_j)\coth\pi\gamma}{1 - i\tan\pi(j+1/2-\rho_j)\coth\pi\gamma} e^{-\pi i(j+1/2-\rho_j)}, \qquad (4.2.3)$$

where

$$\rho_j = \sqrt{(j+1/2)^2 - \gamma^2}$$

$$\gamma = z\alpha = z/137.$$

Equation (4.2.1) and equation (4.2.3) then determine the right side of equation (4.2.2) explicitly so that $\eta_j - \eta_j^c$ can be evaluated.

One more function, η_j^c, needs to be computed before the scattering amplitude series can be summed.

$$\exp 2i\eta_j^c = \frac{\rho_j - i\gamma}{j+1/2} \frac{\Gamma(\rho_j - i\gamma)}{\Gamma(\rho_j - i\gamma)} e^{\pi i(j+1/2-\rho_j)}. \qquad (4.2.4)$$

In general $\eta_j^c = \alpha + i\beta$; $\Gamma(z)$ is the complex Gamma function.

The computer program is designed to generate the following two sets of scattering amplitude series coefficients:

$$(j+1/2)\exp 2i\delta_j \equiv \exp 2i(\eta_j - \eta_j^c) \qquad (4.2.5)$$

where $l = j - 1/2$ for $l = 0,1,2,$

and

$$(j+1/2)\exp 2i\eta_j^c \qquad j = 1/2 \cdots, 29/2 \qquad (4.2.6)$$

These two sets of coefficients, then, allow the following two series to be summed:

$$2ik(f - f_c) = \sum_{j=1/2}^{5/2} (j+1/2)(\exp 2i\delta_j - 1)\exp 2i\eta_j^c \left[P_{j+1/2}(z) + P_{j-1/2}(z) \right] \qquad (4.2.7)$$

and

$$2ikf_c = \sum_{j=1/2}^{29/2} (j+1/2)\exp 2i\eta_j \left[P_{j+1/2}(Z) + P_{j-1/2}(Z) \right] \quad \text{or,}$$

$$= \sum_{l=0}^{14} a_l^{(o)} P_l(Z), \qquad (4.2.8)$$

$Z = \cos\theta$, where $P_l(z)$ are Legendre functions, and the $a_l^{(o)}$ are coefficients explicitly determined from equation (4.2.6). The series (4.2.8) does not converge rapidly so that an "mth reduction" technique, suggested by Yennie, Ravenhall, and Wilson (34), is used, and the computation of f_c is done on the following series instead of series (4.2.8):

$$2ikf_c = \sum_{l=0}^{11} a_l^{(3)} P_l(Z).$$

The superscript on $a_l^{(3)}$ denotes the number of reductions. The equation (4.2.9) defines the function which is plotted against the experimental data:

$$k^2\sigma(\theta) = |f_c + (f - f_c)|^2 \sec^2\frac{\theta}{2} \; . \qquad (4.2.9)$$

Table 6 shows numerical results obtained from A.E. Glassgold (35) which are compared to the computations described above. For the case of the homogeneous distribution there are discrepancies of order 12 percent at the back scattering angles. Taking five phase shifts instead of three, or using integration steps of size $\Delta x = 0.05$ instead of $\Delta x = 0.1$ for the numerically integrated solutions to the Dirac equation does not resolve the discrepancy. The computer calculations for the shell distribution of charge also shows discrepancies of order 12 percent at back angles when compared with those of Glassgold (35).

In order to determine the source of the discrepancy, Glassgold (36) has given the four phase shifts for $Z = 74$ and $kR_h = 2.0$. They are shown in Table 7 along with the corresponding phase shifts from the cal-

culations performed for the present experiment. The table shows that the fourth phase shifts disagree by a factor of 10.

TABLE 6

COMPARISON OF RESULTS OF PRESENT CALCULATION WITH RESULTS OF GLASSGOLD FOR Z = 74 AND kR_h (HOMOGENEOUS MODEL) = 2.0

	$k^2 \sigma(\theta)$		
θ	Naymik	Glassgold	Glassgold & Naymik
50°	1.421	1.424	1.427
55°	8.17 (-1)*	8.19 (-1)	8.21 (-1)
60°	4.75 "	4.75 "	4.77 "
65°	2.78 "	2.78 "	2.79 "
70°	1.64 "	1.632 "	1.641 "
75°	9.72 (-2)	9.68 (-2)	9.72 (-2)
80°	5.81 "	5.73 "	5.80 "
85°	3.51 "	3.53 "	3.53 "
90°	2.15 "	2.20 "	2.19 "
95°	1.35 "	1.394 "	1.409 "
100°	8.80 (-3)	9.12 (-3)	9.45 (-3)
105°	5.96 "	6.13 "	6.58 "
110°	4.22 "	4.20 "	4.71 "
115°	3.10 "	2.94 "	3.43 "
120°	2.36 "	2.15 "	2.49 "
125°	1.83 "	1.621 "	1.795 "
130°	1.44 "	1.273 "	1.266 "

*(-1) means x 10^{-1} .

TABLE 7

PHASE SHIFTS FOR Z = 74 AND kR_h = 2.0 (HOMOGENEOUS MODEL)

j	Naymik	Glassgold
1/2	-4.398 (-1)*	-4.398 (-1)
3/2	-5.071 (-2)	-5.082 (-2)
5/2	-3.544 (-3)	-3.425 (-3)
7/2	-1.52 (-4)	-1.62 (-3)

*(-1) means x 10^{-1} .

By using Glassgold's four phase shifts, summing the scattering amplitude series, and calculating the cross section, one obtains the results shown

in Column 4 of Table 6. The discrepancies between these results (Column 4 of Table 6) and Glassgold's results (Column 3 of Table 6) are still of the order of 10 percent. Figure 19 is a graph showing the curves plotted with the numbers from Table 6. Glassgold's (37) calculation differs from the one reported in this work since he uses desk computers rather than a digital computer, and his Coulomb functions are calculated from a technique developed by Feshbach (4). Coulomb functions for this work were calculated by following Yennie, Ravenhall, and Wilson (34) and checked against a tabulation of Glassgold (38). On the other hand, if the phase shifts for $Z = 79$ and $kR_h = 4.0$ are calculated, by using the digital computer, one obtains the results listed in Table 8. Included in this table are the results obtained from Table 1 of Yennie, Ravenhall, and Wilson (34).

TABLE 8

PHASE SHIFTS FOR $Z = 79$ and $kR_h = 4.0$ (HOMOGENEOUS MODEL)

j	Naymik	Yennie *et al**
1/2	-.85815	-.85820
3/2	-.27136	-.27143
5/2	-.07631	-.07633
7/2	-.01495	-.01494
9/2	-.00198	-.00199
11/2	-.00019	-.00017
13/2	-.00001	-.00001
15/2	-.00000	-.00000
17/2	-.00000	-.00000

*Table 1, Yennie *et al* (34).

Comparison of Experimental Data to Theoretical Calculations

First, the computer calculations for the quantity, $k^2\sigma(\theta)$, which is a function of the scattering cross section, are "normalized" and tabulated in Table 9 for several values of the parameter, kR_h. For

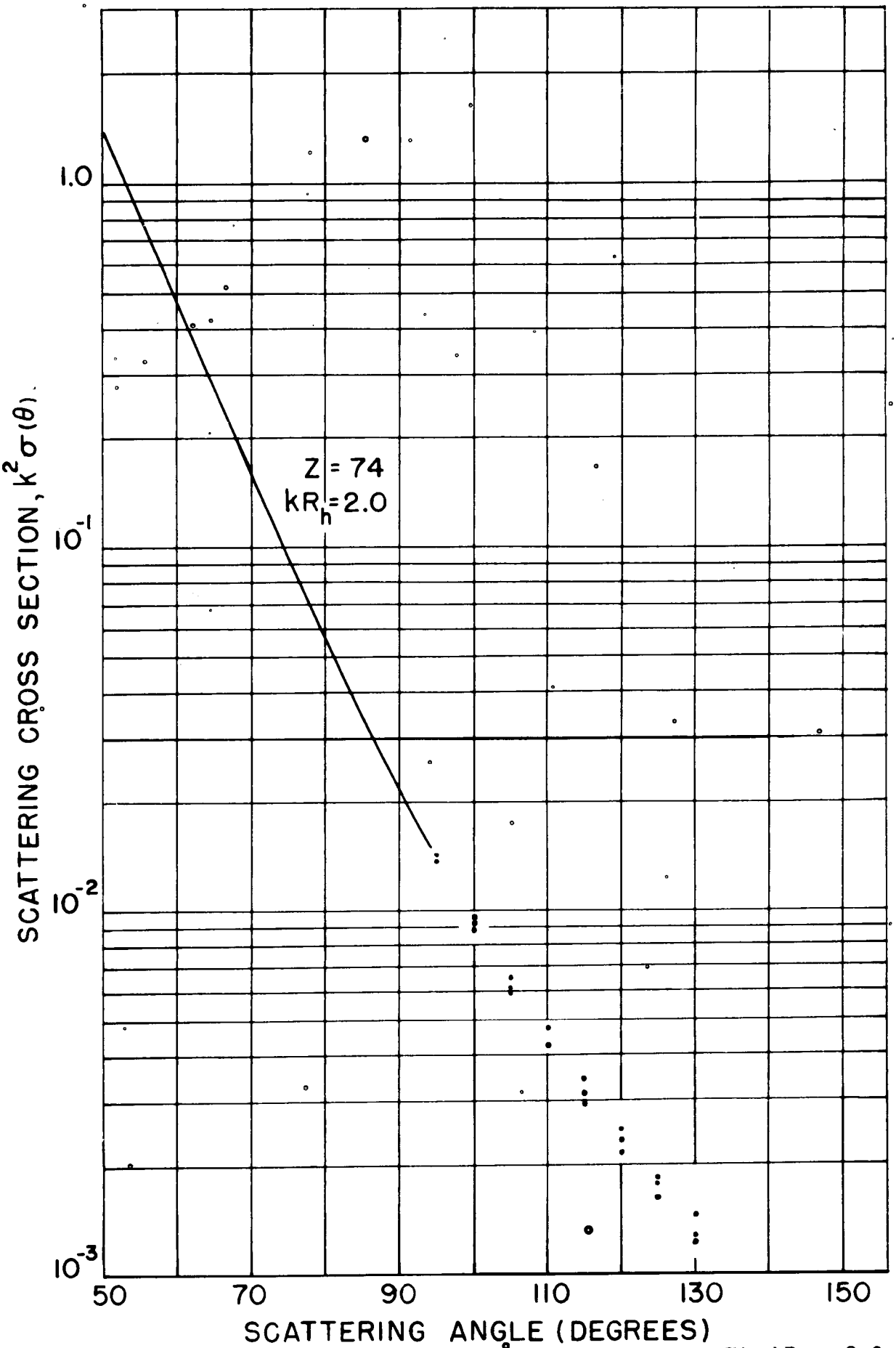


Figure 19. Theoretical Scattering Cross Sections for Z = 74, kR_h = 2.0.

tungsten and copper the "normalization" is relative to 52°, and for aluminum the "normalization" is relative to 65.5° .

Secondly, the experimental data (Tables 2 and 3) are averaged for each scattering angle and each target. In most situations there are five counting runs at each scattering angle which are used to determine an average. This average is divided by the monitor count, N_m, accumulated during each of these five counting runs, normalized in the same manner as the computations of Table 9, and tabulated in Table 10. Estimates of the standard deviations corresponding to these averages are calculated and put into Table 11.

Finally, the experimental data (Table 10) are plotted against the theoretical cross section (Table 9). Since the scattering cross section is a function of the parameter kR_h, the method of least squares can be applied to the experimental data in order to determine the theoretical curve which best fits the experimental data. That value of the parameter, corresponding to the curve of best fit, is then substituted into the following equation:

$$kR_h = \frac{E}{\hbar c} \times r_o A^{1/3} \times 10^{-13} \text{ cm} .$$

Every quantity, except r_o is known in the equation. In this fashion the value of r_o is determined for each of the three target nuclei and is tabulated in Table 12.

Figures 20, 21, and 22 show a graphical comparison of the experimental data with the "best-fitting" curves obtained from the computer calculations. Additional curves are plotted in each figure in order to demonstrate the magnitude of the error that may be attached to the value of r_o for tungsten, copper, and aluminum.

Figure 23 contains a plot of the function which is used to

TABLE 9

TUNGSTEN, COPPER, AND ALUMINUM SCATTERING CROSS SECTIONS FOR HOMOGENEOUS MODEL (NORMALIZED)

θ	kR = 1.9	kR = 2.0	kR = 2.1
Tungsten			
52.0°	1.000	1.000	1.000
65.5°	2.448 (-1)*	2.320 (-1)	2.193 (-1)
76.75°	7.920 (-2)	7.135 (-2)	6.414 (-2)
89.25°	2.365 (-2)	2.031 (-2)	1.755 (-2)
103.25°	6.931 (-3)	5.928 (-3)	5.235 (-3)
116.25°	2.769 (-3)	2.519 (-3)	2.396 (-3)
128.0°	1.445 (-3)	1.401 (-3)	1.400 (-3)
Copper	kR = 1.3	kR = 1.4	kR = 1.5
52.0°	1.000	1.000	1.000
65.5°	3.220 (-1)	3.120 (-1)	3.015 (-1)
76.75°	1.375 (-1)	1.291 (-1)	1.206 (-1)
89.25°	5.670 (-2)	5.121 (-2)	4.580 (-2)
103.25°	2.195 (-2)	1.389 (-2)	1.600 (-2)
116.25°	9.256 (-3)	7.602 (-3)	6.096 (-3)
128.0°	4.213 (-3)	3.319 (-3)	2.532 (-3)
Aluminum	kR = 1.2	kR = 1.3	k = 1.4
52.0°	3.005	3.082	3.168
65.5°	1.000	1.000	1.000
76.75°	4.434 (-1)	4.327 (-1)	4.212 (-1)
89.25°	1.922 (-1)	1.820 (-1)	1.713 (-1)
103.25°	7.924 (-2)	7.239 (-2)	6.542 (-2)
116.25°	3.554 (-2)	3.138 (-2)	2.727 (-2)
128.0°	1.708 (-2)	1.464 (-2)	1.228 (-2)

*(-1) means x 10^{-1} .

TABLE 10

UNCORRECTED AND NORMALIZED EXPERIMENTAL COUNTING RATES (COUNTS PER MONITOR COUNT)

θ	Tungsten	Copper	Aluminum
52.0°	1.000	1.000	3.767
65.5°	2.284 (-1)*	3.000 (-1)	1.000
76.75°	7.176 (-2)	1.192 (-1)	3.943 (-1)
89.25°	2.220 (-2)	4.618 (-2)	1.453 (-1)
103.25°	6.935 (-3)	1.833 (-2)	7.368 (-2)
116.25°	2.573 (-3)	6.671 (-3)	3.201 (-2)
128.0°	1.342 (-3)	3.497 (-3)	1.524 (-2)

*(-1) means x 10^{-1} .

TABLE 11

UNCORRECTED AND NORMALIZED DEVIATIONS TO EXPERIMENTAL COUNTING RATES (COUNTS PER MONITOR COUNT)

θ	Tungsten	Copper	Aluminum
52.0°	.08	.05	.14
65.5°	.09 (-1)*	.09 (-1)	.12
76.75°	.20 (-2)	.02 (-1)	.31 (-1)
89.25°	.05 (-2)	.16 (-2)	.06 (-1)
103.25°	.17 (-3)	.01 (-2)	.15 (-2)
116.25°	.06 (-3)	.13 (-3)	.41 (-2)
128.0°	.06 (-3)	.19 (-3)	.05 (-2)

*(-1) means x 10^{-1}.

TABLE 12.

VALUES OF r_o FOR TUNGSTEN, COPPER, AND ALUMINUM

	r_o	kR_h	$0.775\ kR_h = kR_s$
Tungsten	1.14 ± .06	2.0	1.550
Copper	1.15 ± .06	1.4	1.085
Aluminum	1.41 ± .07	1.3	1.008

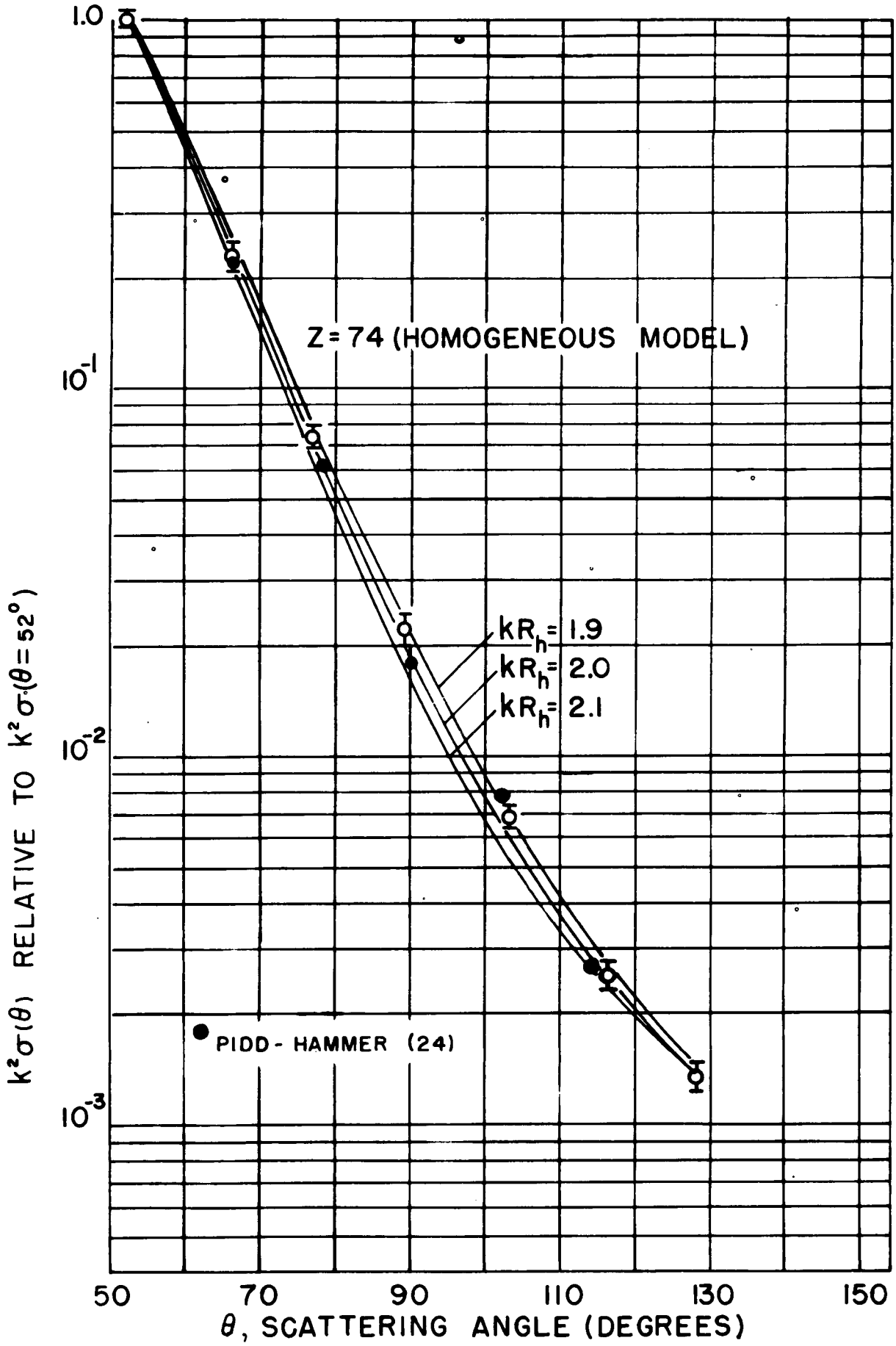


Figure 20. Experimental Points and Theoretical Curves for Tungsten (Homogeneous Model).

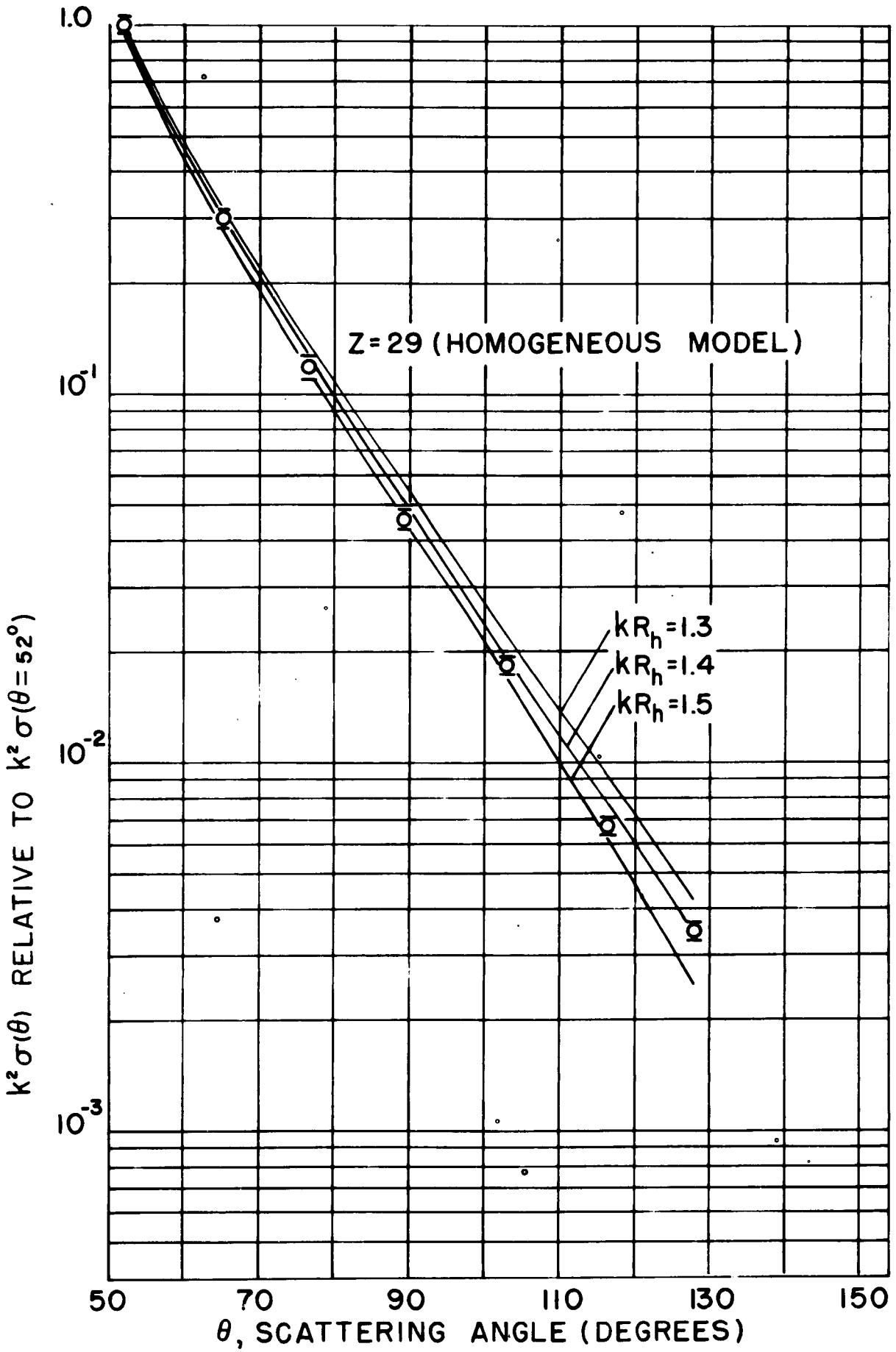


Figure 21. Experimental Points and Theoretical Curves for Copper (Homogeneous Model).

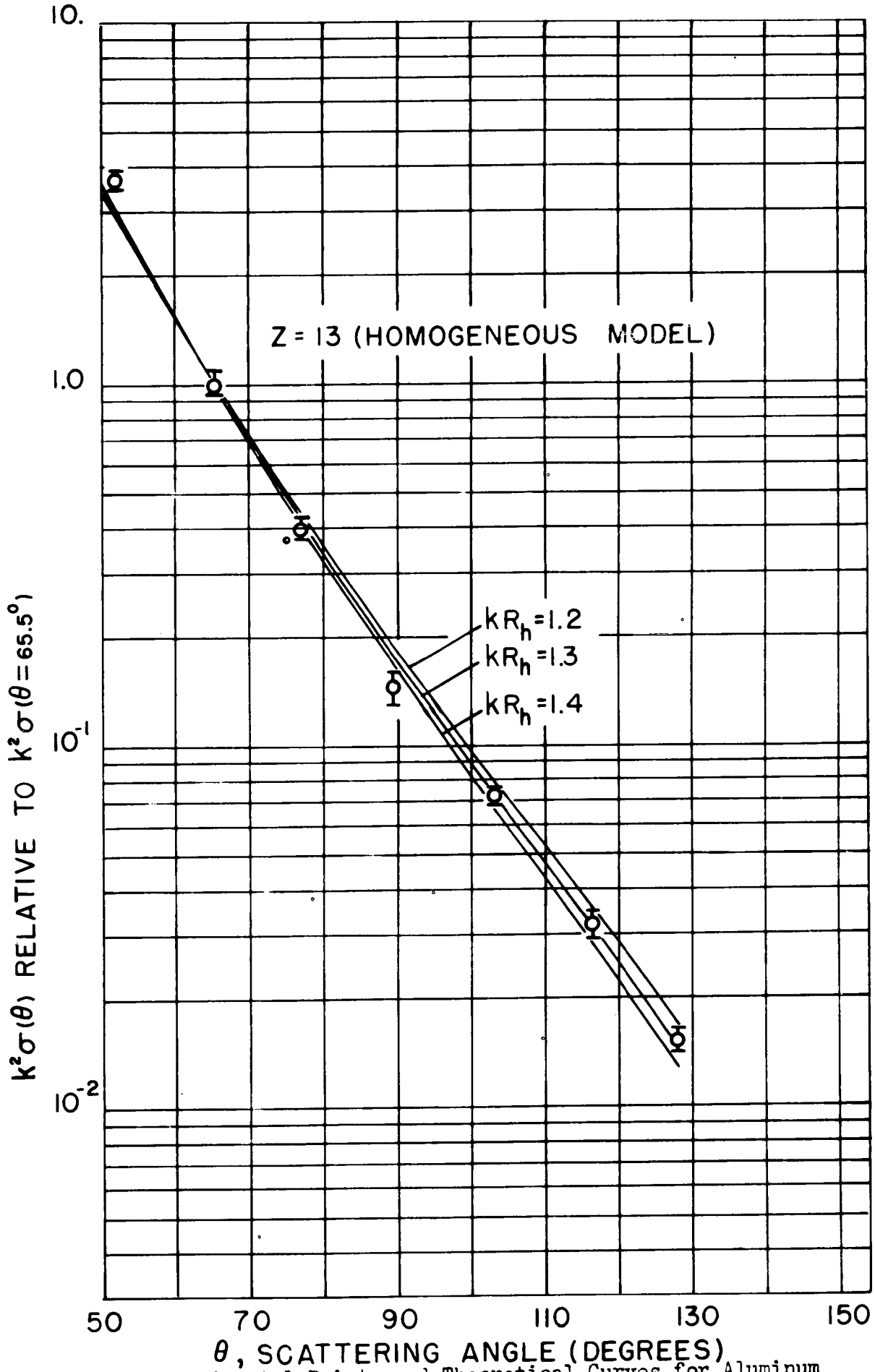


Figure 22. Experimental Points and Theoretical Curves for Aluminum (Homogeneous Model).

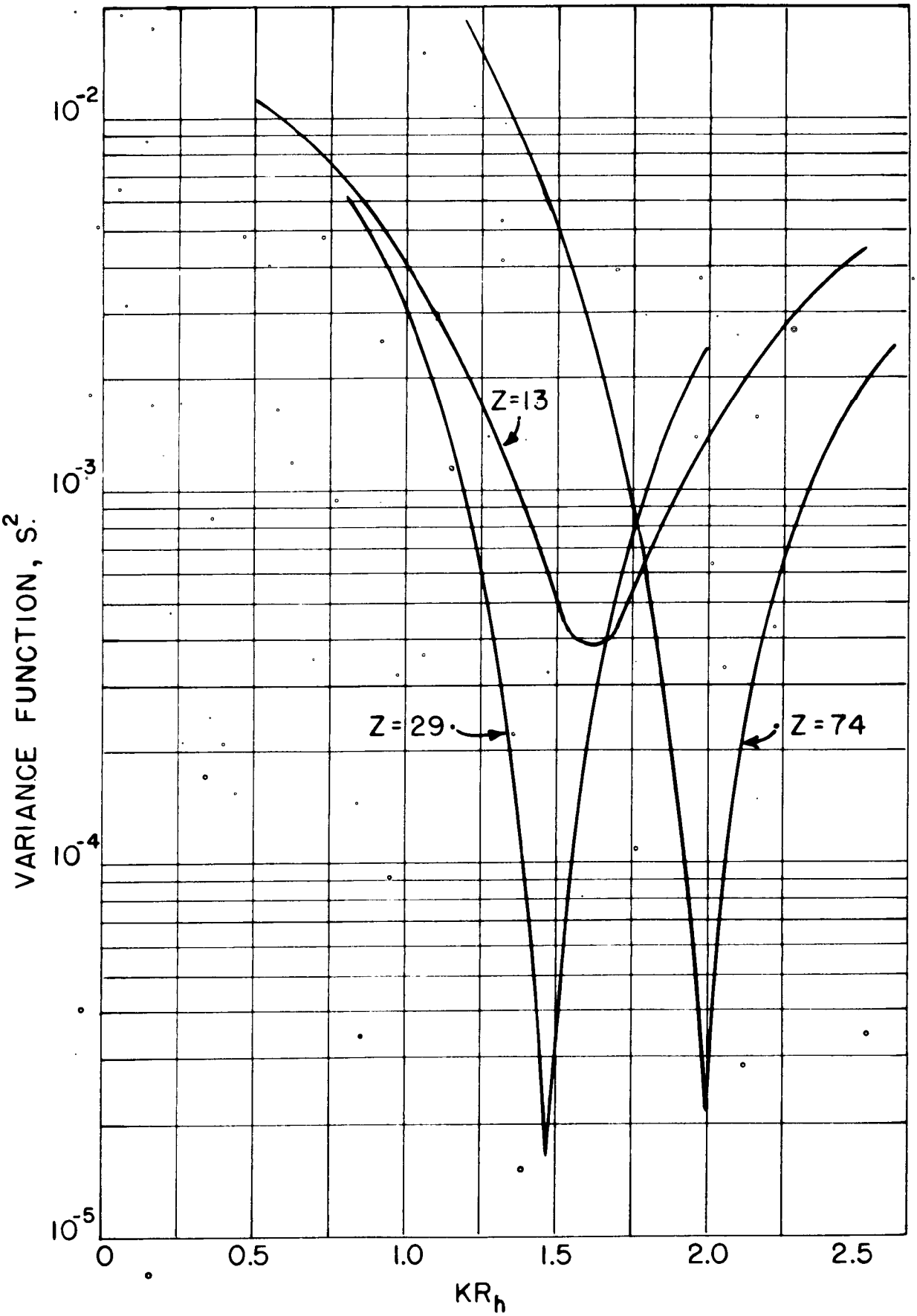


Figure 23. Least Square Fit of Experimental Data (Homogeneous Model).

determine that value for the parameter kR_h corresponding to the "best-fitting" curve. This function is

$$S^2 = \frac{1}{6} \sum_{i=1}^{7} \left[\lambda n(\theta_i) - k^2 \sigma(\theta_i)\right]^2,$$

where

$n(\theta_i)$ is the experimental counting rate relative to the angle, 52°,

$\sigma(\theta_i)$ is the theoretical cross section relative to 52°,

k is the wave number of the incident electron, and

θ_i is the experimentally measured scattering angle,

$i = 1 \ldots 7$, and λ is the normalizing factor.

The function, S^2, is an estimate of the statistical parameter called variance; it measures the accuracy of the measurements made in this experiment. In fact, reference to Figure 23 shows that part of the experimental data for aluminum requires statistical analysis in order to determine whether or not these data are a result of statistical fluctuations; this will be discussed in the next section on statistical analysis.

The method of least squares is also applied to the experimental data using the shell model calculations which are tabulated in Table 13 and plotted in Figures 24, 25, and 26. Curves similar to those shown in Figure 23 are obtained; however, the minimum of the function, S^2, for $Z = 74$ was less for the homogeneous model calculations than for the shell model calculation. One can conclude, therefore, that for tungsten the homogeneous model of nuclear charge is more compatible with the experimental data than the shell model; no such statement, however, can be made about the experimental data of copper and aluminum.

Feshbach (9) has shown that for low energies, where the wave-

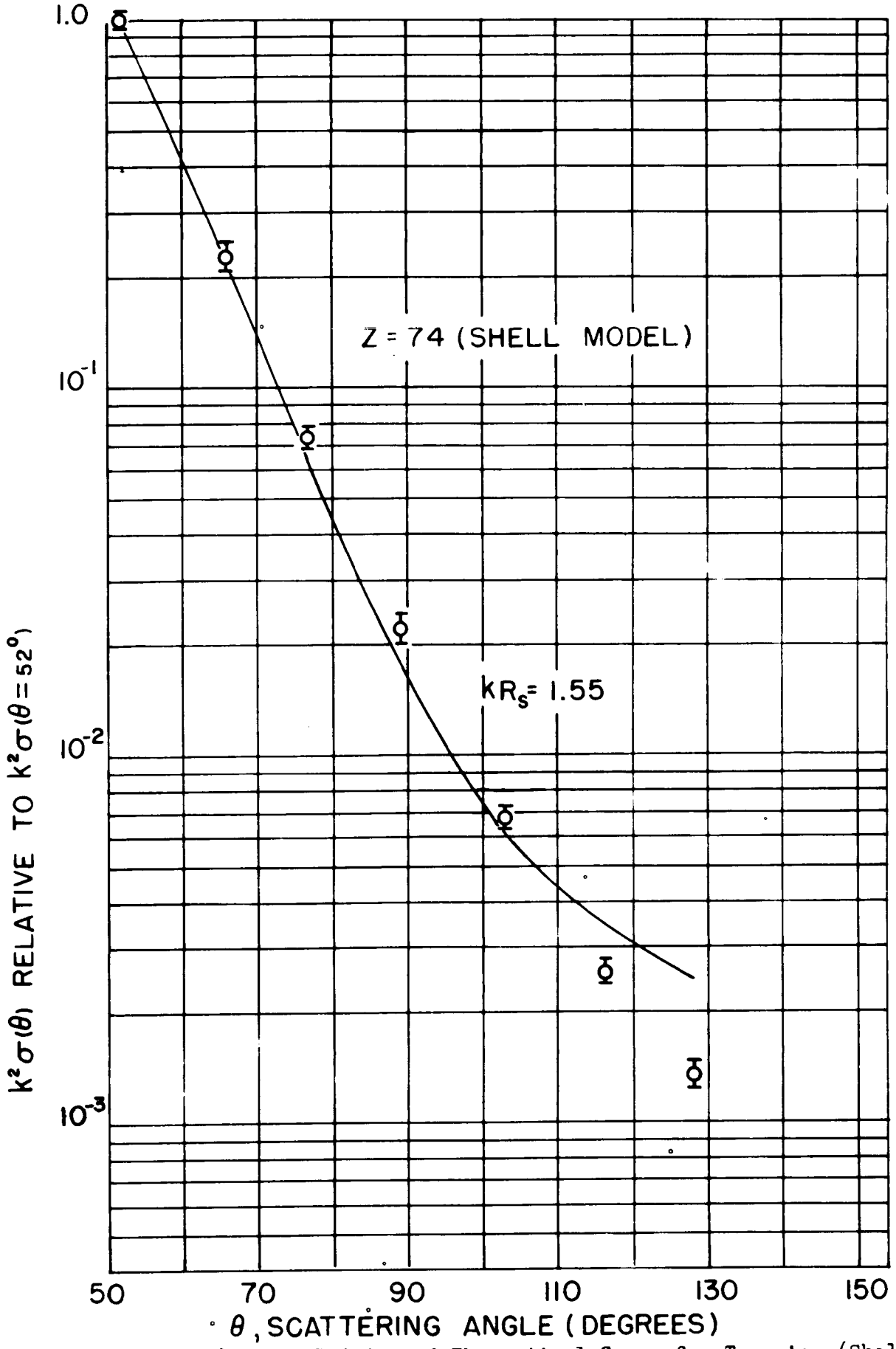


Figure 24. Experimental Points and Theoretical Curve for Tungsten (Shell Model).

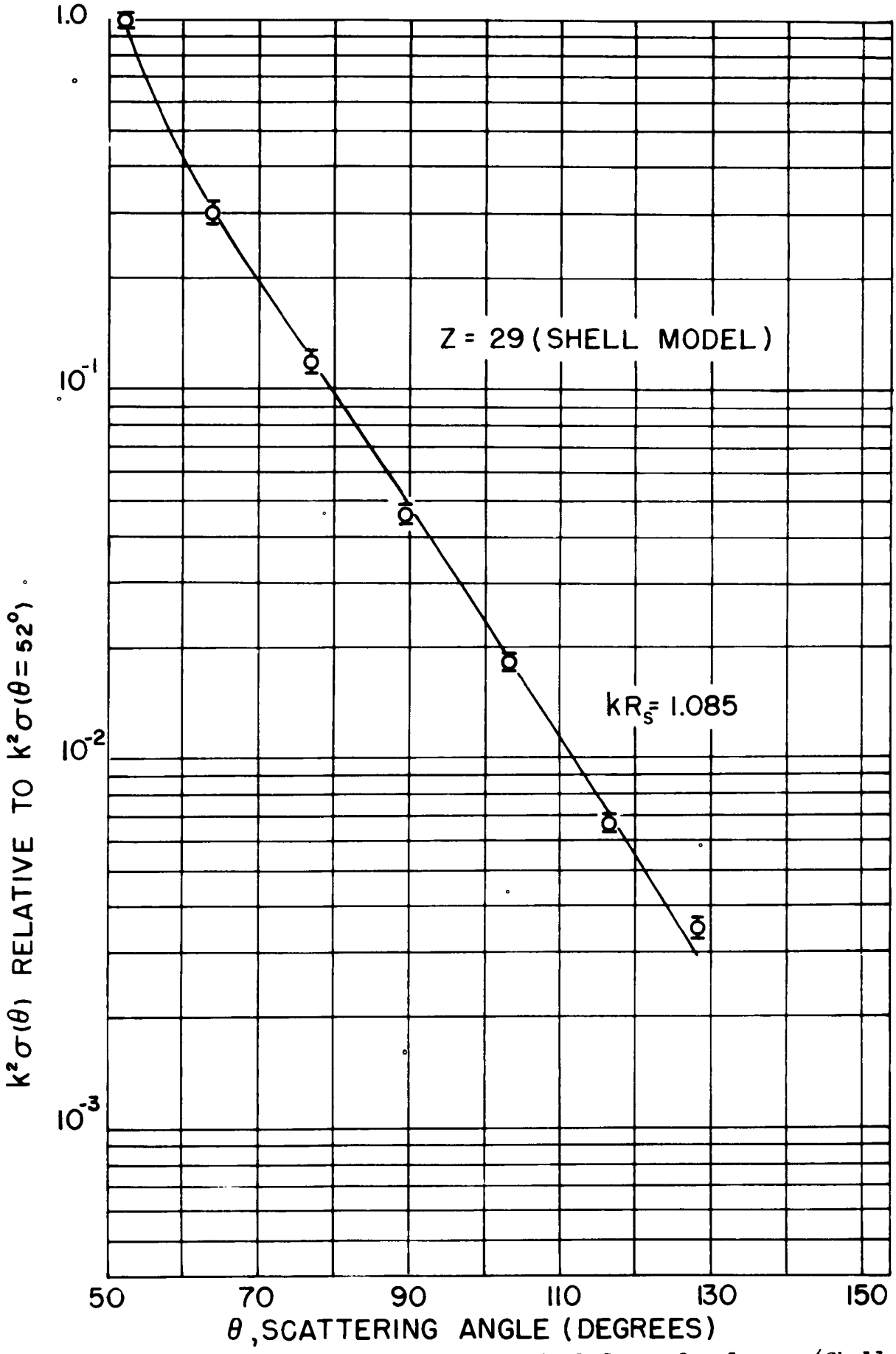


Figure 25. Experimental Points and Theoretical Curve for Copper (Shell Model).

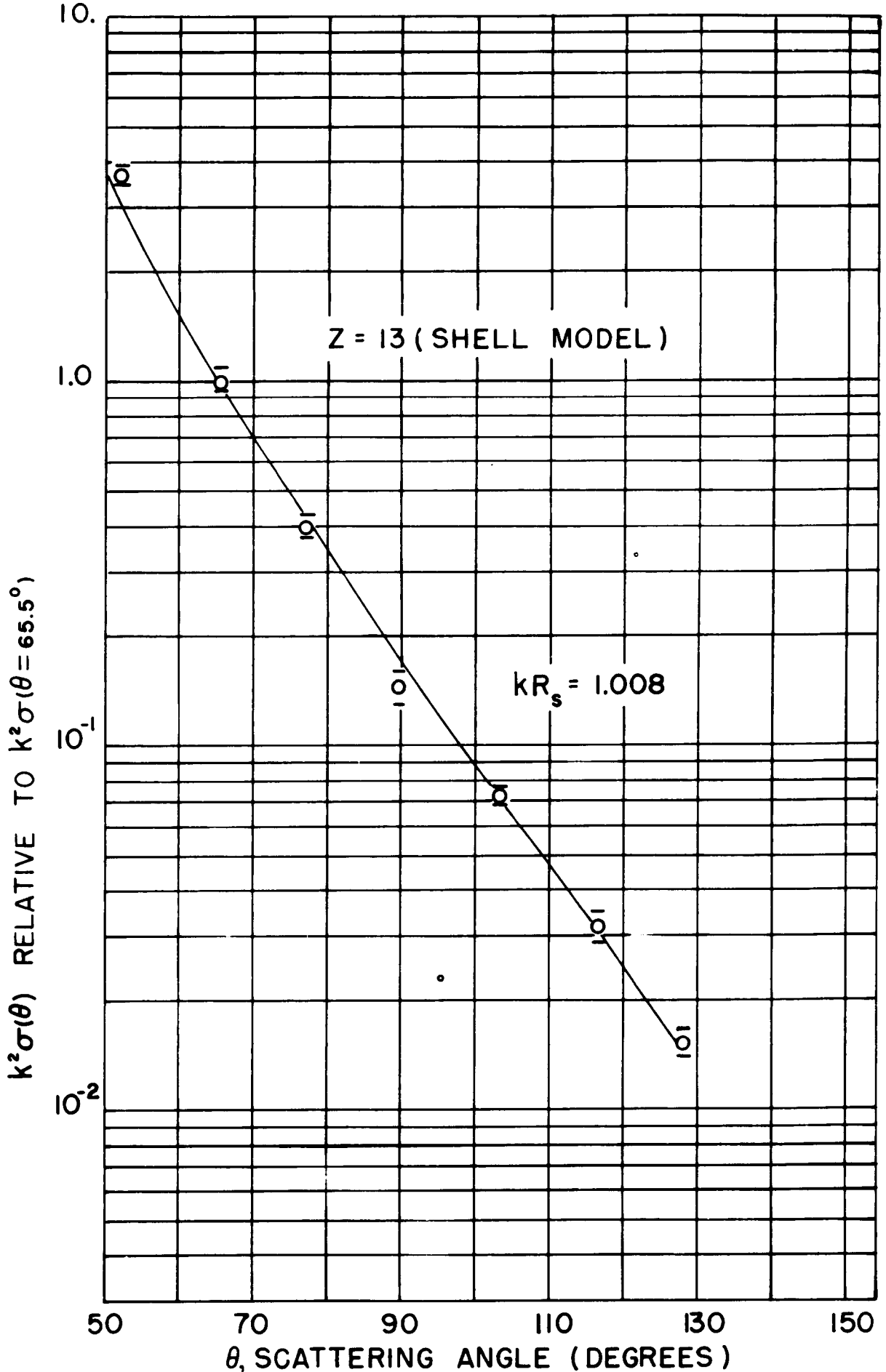


Figure 26. Experimental Points and Theoretical Curve for Aluminum (Shell Model).

TABLE 13

TUNGSTEN, COPPER, AND ALUMINUM SCATTERING CROSS SECTIONS FOR SHELL MODEL (NORMALIZED)

θ	Z = 74 kR = 1.550	Z = 29 kR = 1.085	Z = 13 kR = 1.008
52.0°	1.00	1.00	3.09
65.5°	2.20 (-1)*	3.10 (-1)	1.00
76.75°	6.37 (-2)	1.27 (-1)	4.30 (-1)
89.25°	1.75 (-2)	4.95 (-2)	1.79 (-1)
103.25°	6.08 (-3)	1.78 (-2)	7.04 (-2)
116.25°	3.59 (-3)	6.94 (-3)	3.00 (-2)
128.0°	2.48 (-3)	2.94 (-3)	1.38 (-2)

*(-1) means x 10^{-1} .

length of the electron is large compared to the dimensions of the target nucleus, that the experimental scattering data can be characterized by specifying only one phase shift. The invariance of the root mean square radius, the second moment of the charge distribution, implies that two different models of nuclear charge distributions will have the same first phase shift. In other words, the scattering is "model independent." Reference to Table 12 and Figures 24, 25, and 26 shows that the shell model curves for values of kR_s which satisfy the relation, $kR_s = 0.775\ kR_h$, should be compared to the experimental data. The relation between R_s, radius of the nucleus for the shell model, and R_h, radius of the nucleus for the homogeneous model, comes from the requirement that the root mean square radius be the same for both nuclear charge distributions.

Statistical Analysis

The seemingly poor quality of the aluminum experimental data requires statistical analysis in order to evaluate the two aluminum data

obtained for the scattering angles, 52° and 89.25°. For this analysis the r-statistic is chosen because (1) the 21 data do not have the same mean, and (2) there are 7 groups of 3 data each that have different standard deviations. The r-statistic is suitable in this situation because it is independent of both the mean value and the standard deviation parameters and is dependent only on the number of data in the experiment.

Arley and Buch (39) have tabulated the r-distribution function which is given by

$$\phi(r)\,dr = \frac{1}{\sqrt{\pi(f+1)}} \frac{\left[\frac{f-1}{2}\right]!}{\left[\frac{f-2}{2}\right]!} \left[1 - \frac{r^2}{f+1}\right]^{\frac{f-2}{2}} dr, \qquad |r| = \sqrt{f+1}$$

where $n = f - 1$ is the number of measurements,

$$\hat{r}_i = \sqrt{n}\ \frac{G(\hat{x}_i) - \hat{m}}{\hat{q}}$$

$$\hat{m} = \frac{1}{n}\left[G(\hat{x}_1) + \cdots + G(\hat{x}_n)\right], \qquad \text{and}$$

$$\hat{q}^2 = \sum_{i=1}^{n} \left[G(\hat{x}_i) - \hat{m}\right]^2.$$

The quantity, x_i, is the ith measurement. The caret above a symbol denotes "random variable," and the same symbol without a caret is one of a possible number of values that the random variable may have.

In this experiment $G(\hat{x})$ is the relative deviation of the measurement from the corresponding theoretical cross section, and the results of computing r_i $(i = 1 \ldots 21)$ are listed for two sets of kR values in Table 14. If one chooses the 10 percent confidence limits, reference to a table of the r-distribution function will show that

$$\text{Prob}\left\{|r_i| > 1.649\right\} = 0.10;$$

that is, 10 percent of the data should give an r-value greater than

1.935. According to Table 14 this is the case so that one can conclude that the 52° and 89.25° points in the aluminum data do not fit the theoretical curves because of statistical fluctuations; at least such a conclusion is a possible one.

TABLE 14

VALUES OF THE r-STATISTIC FOR HOMOGENEOUS MODEL

r_i	Z = 74, kR = 2.0 Z = 29, kR = 1.4** Z = 13, kR = 1.3	Z = 74, kR = 2.0 Z = 29, kR = 1.5 Z = 13, kR = 1.3
i = 1	3.92 (-2)*	-3.91 (-1)
2	-1.22 (-1)	-5.19 (-1)
3	9.90 (-2)	-3.44 (-1)
4	1.00	3.73 (-1)
5	1.80	1.00
6	2.62 (-1)	-2.14 (-1)
7	-3.93 (-1)	-7.33 (-1)
8	3.92 (-2)	-3.91 (-1)
9	-3.58 (-1)	-4.30 (-1)
10	-7.62 (-1)	-4.88 (-1)
11	-9.82 (-1)	-3.22 (-1)
12	-2.72 (-1)	8.05 (-1)
13	-1.23	3.84 (-1)
14	5.99 (-1)	2.74
15	2.35	1.43
16	3.92 (-2)	-3.91 (-1)
17	-8.83 (-1)	-1.12
18	-2.05	-2.05
19	2.24 (-1)	-2.45 (-1)
20	2.48 (-1)	-2.26 (-1)
21	4.68 (-1)	-5.26 (-2)

*(-2) means x 10^{-2} .

**Parameter corresponding to the curve of "best fit."

In Table 14 an additional column (column 3) has been added in order to show the effect of a 10 percent change in the kR value for copper. This change shows that the last datum for copper (entry 14) instead of the first datum for aluminum (entry 15), now lies outside the

10 percent confidence limit.

Conclusion

The results from this experiment indicate that r_o for tungsten almost agrees with the measurements made by Hammer (10) who quotes $r_o = 1.04 \pm .07$ fermis for tungsten at the beam energies of 33 and 43 mev. The value of $1.21 \pm .18$ for r_o reported by Pidd and Hammer (24) is in fair agreement with the value, $1.14 \pm .06$ fermis, resulting from the present measurement. Measurements by Hahn et al (14) using heavy nuclei, such as gold, have given r_o a value of 1.18 ± 0.02 to nuclei with atomic numbers near that of tungsten.

No previous data have been published for aluminum or copper for energies in any range near 60 mev. However, mirror nuclei measurements, using $_{13}Al^{27}$, by Carlson and Talmi (40) give the value for r_o as $1.197 \pm .002$ which is not comparable to the value of $1.41 \pm .07$ obtained for aluminum in this experiment.

The disagreement between these two measurements is not disturbing because electron scattering is a method of determining r_o which is different from the mirror nuclei measurements; consequently, these two methods of measurement may not be evaluating the same quantity. Carlson and Talmi base their calculation on the nuclear shell model theory in which a modified harmonic oscillator potential energy is used. They point out, however, that appreciably larger values for r_o are obtained if a uniform model of nuclear charge distribution is assumed. The discrepancies between these models seem to be due, partially, to the absence of "exchange effects" in the homogeneous model calculations for the Coulomb energies of mirror nuclei. Helm (16) has measured r_o for $_{12}Mg^{24}$ which is a nucleus of nearly the same Z and A as $_{13}Al^{27}$. His

results were obtained from 183 mev data and show that $r_o = 1.33 \pm .03$, which is in much better agreement with the value, $1.41 \pm .07$, quoted in the present work than the results of Carlson and Talmi.

Reference to the Figures 20 and 23 shows that the experimental data for tungsten, only, can distinguish between shell model and homogeneous model calculations. Within the accuracy of this measurement electron scattering from copper and aluminum is "model independent" at the electron energy of 60.6 mev.

BIBLIOGRAPHY

1. Rutherford, E.R., Radiations from Radioactive Substances, Cambridge University Press, Cambridge (1930), Chapter 9, p. 280.

2. Lyman, E.M., Hanson, A.O., and Scott, M.B., Phys. Rev., 84, 626 (1951).

3. Acheson, L.K. Jr., Phys. Rev., 82, 488 (1951).

4. Feshbach, H., Phys. Rev., 88, 295 (1952).

5. Elton, L.R.B., Proc. Phys. Soc., A 63, 1115 (1950).

6. Rose, M.E., Phys. Rev., 73, 279 (1948).

7. Parzen, G., Phys. Rev., 80, 355 (1950).

8. Pidd, R.W., Hammer, C.L., and Raka, E.C., Phys. Rev., 92, 436 (1953).

9. Feshbach, H., Phys. Rev., 84, 1206 (1951).

10. Hammer, C.L., Thesis, University of Michigan (1953).

11. Raka, E.C., Thesis, University of Michigan (1953).

12. Hofstadter, R., Rev. mod. Phys., 28, 214 (1956).

13. Hofstadter, R., Ann. Rev. Nucl. Sci., 7, 231 (1957).

14. Hahn, B., Ravenhall, D.G., and Hofstadter, R., Phys. Rev., 101, 1131 (1956).

15. Downs, B.W., Ravenhall, D.G., and Yennie, D.R., Phys. Rev., 106, 1285 (1957).

16. Helm, R.H., Thesis, Stanford University (1956).

17. Fregeau, J.H. and Hofstadter, R., Phys. Rev., 99, 1503 (1955).

18. Fregeau, J.H., Thesis, Stanford University (1956).

19. McAllister, R.W., and Hofstadter, R., Phys. Rev., 102, 851 (1956).

20. Rosenbluth, M.N., Phys. Rev., 79, 615 (1950).

21. Chambers, E.E., and Hofstadter, R., Phys. Rev., 103, 1454 (1956).

BIBLIOGRAPHY-Continued

22. McIntyre, J.A., and Hofstadter, R., Phys. Rev., 98, 158 (1955).

23. McIntyre, J.A., Phys. Rev., 103, 1464 (1956).

24. Pidd, R.W., and Hammer, C.L., Phys. Rev., 99, 1396 (1955).

25. Randolph, P.D., Thesis, University of Michigan (1958).

26. Cline, J.E., Thesis, University of Michigan (1958).

27. Heitler, W., The Quantum Theory of Radiation, Oxford University Press, Oxford (1947), p. 168.

28. Westcott, C.H., Proc. Roy. Soc., A 194, 508 (1948).

29. Molière, G., Z. Naturforsch, 3a, 78 (1948).

30. Goudsmit, S.A., and Saunderson, J.L., Phys. Rev., 57, 24 and 58, 36 (1940).

31. Bethe, H.A., Phys. Rev., 89, 1256 (1953).

32. Chase, C.T., and Cox, R.T., Phys. Rev., 58, 243 (1940).

33. Hanson, A.O., Lanzl, L.H., Lyman, E.M., and Scott, M.B., Phys. Rev., 84, 634 (1951).

34. Yennie, D.R., Ravenhall, D.G., and Wilson, R.N., Phys. Rev., 95, 500 (1954).

35. Glassgold, A.E., Private Communication.

36. Glassgold, A.E., Private Communication.

37. Glassgold, A.E., Phys. Rev., 98, 1360 (1955).

38. Glassgold, A.E., and Mack, Evelyn W., Technical Report No. 65, Office of Naval Reserve (1954).

39. Arley, N. and Buch, K.R., Introduction to the Theory of Probability and Statistics, John Wiley & Sons, New York (1950), pp. 98, 217.

40. Carlson, B.C., and Talmi, I., Phys. Rev., 96, 436 (1954).